RESEARCH ARTICLE

VOLCANICA

Characteristics of ash particles from the maar complex of Lamongan Volcanic Field (LVF), East Java, Indonesia: How textural features and magma composition control ash morphology

Muhammad Andriansyah Gurusinga*[α], Tsukasa Ohba[α], Agung Harijoko[β], and Takashi Hoshide[α]

[α] Department of Earth Resource Science, Akita University, 1-1, Tegata Gakuenmachi, Akita 010-8502, Japan.
[β] Department of Geological Engineering, Faculty of Engineering, Universitas Gadjah Mada, Jalan Grafika no 2, Yogyakarta 55281, Indonesia.

Submitted: 2023-03-06 | Accepted: 2023-09-15 | Published: 2023-11-15

Editor: A. H. Graettinger | Typesetter: J. Farquharson

Abstract

The Lamongan Volcanic Field (LVF), East Java, Indonesia, has experienced numerous maar eruptions, producing varied properties and morphologies of ash particles. This study conducted textural, morphometric, and geochemical analyses of the juvenile particles to elucidate the factors governing their heterogeneous characteristics. Two distinct types of juvenile ash were identified: A (black and brown ash) and B (orange-brown ash), reflecting different fragmentation processes. The blocky to slightly elongate shapes of juvenile A across heterogenous basaltic compositions (resulting in variable textures, rheological properties, and/or cooling histories) highlight the phreatomagmatic process as the primary control of their shape. In contrast, the irregular-fluidal shapes of juvenile B particles indicate magmatic fragmentation of basaltic andesite magma. This study reveals that variable magma properties yield diverse ash components, yet fragmentation dynamics govern pyroclast shapes in the LVF maar complex. Our integrated approach emphasizes the importance of considering multiple variables when interpreting heterogeneous volcanic ash deposits.

Abstrak

Kompleks Vulkanik Lamongan (*LVF*), Jawa Timur, Indonesia, telah mengalami sejumlah erupsi gunung api maar yang menghasilkan produk abu vulkanik dengan variasi sifat dan bentuk. Dalam studi ini dilakukan analisis tekstur, morfometrik, dan geokimia pada abu vulkanik untuk menjelaskan faktor-faktor yang memengaruhi keberagaman karakteristiknya. Dua jenis abu vulkanik (*juvenile*) yang berbeda dapat diidentifikasi yaitu: *juvenile A* (abu vulkanik hitam dan cokelat) dan *juvenile B* (abu vulkanik oranye kecokelatan), yang mencerminkan proses fragmentasi yang berbeda. Bentuk *juvenile A* yang *blocky* hingga agak memanjang (*elongate*) berasal dari komposisi basaltik yang heterogen yang berkaitan dengan tekstur, sifat reologi, dan sejarah pendinginan yang bervariasi. Hal ini menunjukkan bahwa proses *phreatomagmatic* memainkan peran utama dalam membentuk karakteristik tersebut. Sebaliknya, bentuk tidak teratur (*irregular*) dan fluidal dari *juvenile B* menunjukkan fragmentasi dari magma basaltik andesit. Studi ini mengungkapkan bahwa sifat magma yang bervariasi menghasilkan komponen abu vulkanik yang beragam, namun dinamika fragmentasi memiliki peranan dalam mengontrol bentuk abu vulkanik dari kompleks maar di *LVF*. Integrasi dari pendekatan yang telah dilakukan dalam studi ini menekankan pentingnya untuk mempertimbangkan berbagai variabel saat mengamati dan menafsirkan endapan abu vulkanik yang heterogen.

Keywords: Volcanic ash; Ash shape; Maar; Phreatomagmatic; Lamongan Volcanic Field.

1 Introduction

Maars are volcanic landforms typically generated by phreatomagmatic eruptions, which occur when magma comes into contact with shallow groundwater, leading to violent, ash-rich explosive eruptions [Sheridan and Wohletz 1983; Lorenz 1986; White and Ross 2011; Smith and Németh 2017; Valentine et al. 2017; Graettinger 2018; Németh and Kósik 2020]. They often occur in groups or fields within multiple craters formed by closely spaced explosions over time [e.g. Lorenz 1986; Jordan 2013; Morales Volosín and Risso 2019]. Maar-forming phreatomagmatic events produce a wide range of pyroclastic particles, each exhibiting distinctive properties and morphologies [Heiken 1978; Sheridan and Wohletz 1983; Wohletz and Sheridan 1983; Dellino and Liotino 2002; Mattsson 2010]. The characteristics of these pyroclastic particles, in particular in the ash size range, are influenced by the fragmentation processes (e.g. brittle vs. ductile) and magma properties (composition, viscosity, temperature, bubbles, and crystals) [Maria and Carey 2002; 2007; Noguchi et al. 2008; Mattsson 2010; Miwa et al. 2013; Liu et al. 2015; Nurfiani and Bouvet de Maisonneuve 2018; Ross et al. 2022], as well as by pyroclast transport [Manga et al. 2011; Kueppers et al. 2012; Jordan 2013; Liu et al. 2015; Hornby et al. 2020]. Despite maar eruptions being driven by magma-water interaction, distinguishing the factors controlling the characteristics of the pyroclasts from maar eruptions remains a challenge. These are attributed to the underlying complexity of phreatomagmatic explosions, which involve dynamic interplay between magmatic properties and the explosivity of magma-water contact [Wohletz and Sheridan 1983; Büttner et al. 2002; Schipper 2009; Pardo et al. 2014]. Consequently, further thorough investigations are required to unravel the key variables governing the heterogeneous characteristics of ash particles in maar volcanoes.

The deposits of the Lamongan Volcanic Field (LVF) maar complex in Indonesia provide an opportunity to evaluate the

* magurusinga11@gmail.com

factors that control the characteristics of ash particles. We investigated particles from the ash-dominated proximal deposits at six maars, where particle modification by secondary processes such as transport is minimized [e.g. Liu et al. 2015; Hornby et al. 2020]. Although previous studies have reported on the physical volcanology and the geochemistry of the LVF [Carn 2000; Carn and Pyle 2001], none have investigated the pyroclast products from the Maar complex. The objective of this study is to provide a comprehensive analysis of ash particles derived from the LVF maar complex, with a primary emphasis on their morphological, textural, and geochemical characteristics [e.g. White and Houghton 2006; Cioni et al. 2008; Ross and White 2012; Rausch et al. 2015]. Through this analysis, we aim to elucidate the underlying variables that govern the variability of ash properties and morphologies generated by maar eruptions.

1.1 Lamongan Volcanic Field (LVF)

Lamongan Volcanic Field (LVF) is located c. 140 km southeast of Surabaya, East Java, Indonesia, and lies between the Tengger-Semeru and Iyang-Argapura volcanic complexes. The LVF and its surroundings are the product of Pleistocene to Holocene volcanism [Suwarti and Suharsono 1992]. Lamongan volcano, the central edifice, consists of three vents: Tarub, Tjupu, and Lamongan (Figure 1). The oldest vent is the truncated Tarub cone. Tjupu is a scoria cone complex that covers several hundred meters between Lamongan and Tarub. Lamongan is a basaltic stratovolcano with an NW–SE linear orientation. It is, to date, the only active vent, with lava flows covering the west and southwest flanks. Although the first historical eruption occurred in 1799 CE, the Lamongan volcano was one of the most active volcanoes in Indonesia during the 19th century. It has undergone around 40 eruptions, including 15 effusive basaltic eruptions [Carn 2000]. Following the last six eruptions in 1898, seismic activity in the west region of the LVF in 1925, 1978, 1985, and 1988–1989 raised awareness of volcanic hazards in this area.

The LVF covers an area of 260 km^2. It comprises several prehistoric centers, including 61 cinder-spatter cones and 29 maars, distributed on the flanks around the central edifice (Figure 1). The maars have variable dimensions (crater diameters from 175 to 575 m) and were formed by eruptions that ejected tephra volumes of 0.02–51 $\times$ 10^6 m^3 dense rock equivalent (DRE) [Carn 2000]. In terms of eruptive rate and volume, Carn [2000] estimated the age of the LVF to range from 40 to 13 ka and placed it among the youngest-dated volcanoes in Indonesia. LVF maar deposits include pyroclastic surges, pyroclastic flows, ash falls, and ballistic ejecta of various sizes.

2 Methods

Ash samples were collected from five crater-wall maar exposures to minimize the influence of the transport process, except for one outcrop situated approximately 200 m NE of Ranu Kembar maar, which was included to supplement the limited outcrops in the eastern region (Figure 1E). In cases where deposits were consolidated, the samples were disaggregated by gently hitting them with a rubber hammer wrapped in a soft fabric. The samples were then manually dry-sieved using a whole-ϕ interval. Subsequently, particles ranging in size from 125–250 µm (+3 to +2 ϕ) from ash-rich layers were selected and subjected to ultrasonic cleaning in order to remove any adhering muddy material. To prevent potential damage to the original ash particles that could arise from prolonged ultrasonic treatment, the cleaning cycles were interrupted, and water was replaced every 60–90 seconds.

Upon completion of the drying process, the samples underwent an epoxy immersion process, following which the lower part of the briquette was polished until the central portion of each grain became visible [Comida et al. 2022]. This polished part was mounted to the glass slide and then prepared into a polished thin section of 30 µm thickness. Polarized light microscopy was utilized to determine the ash components and shapes. Juvenile (black, brown, and orange ash) and other (altered/weathered ash and free crystals) grains were discriminated on the basis of color and internal texture.

To quantify the morphometric parameters of the ash particles in 2D cross-sections, we delineated their outlines on photomicrographs using a vector editing tool (`Corel Draw`). We converted the drawings into black-and-white (binary) TIFF files. Particles were hand-delineated due to the presence of fine aggregate coatings on some grains, which could interfere with automated edge detection. The clast images were processed using Particle Shape Analyzer (`PARTISAN`), a software application developed by Dürig et al. [2018] written in `MATLAB` ®. This yielded image particle analysis (IPA) parameters [Dellino and Volpe 1996] and morphometric parameters from the Liu et al. [2015] system, such as [1] Circularity ($Circ_{\mathrm{DL}}$); [2] Rectangularity (Rec_{DL}); [3] Compactness (Com_{DL}); [4] Elongation (Elo_{DL}) and [5] Form Factor (FF); [6] Axial Ratio (AR_{LI}); [7] Convexity (Con_{LI}); [8] Solidity (Sol_{LI}), respectively.

Furthermore, ash particles were observed using a scanning electron microscope (SEM) of the JEOL JSM-IT300 model at Akita University, both as cross-sections (the thin section mentioned above) and in three dimensions (3D). For the latter method, ash grains from the same size fraction were mounted on a glass slide using carbon tape. Subsequently, both the thin sections and the carbon tape grain mounts were coated with ~30 nm of carbon. The identification of 3D grain morphology and surface features was performed in secondary electron (SE) mode, while petrography and textures of particle cross-section were examined in backscattered electron (BSE) mode. The SEM operation was conducted under high vacuum conditions with a 15 kV accelerating voltage, a 10 mm working distance, and a probe current of 2.20 nA.

Crystals and vesicles were manually digitized from BSE images of the cross-sections using `Corel Draw`, both at relatively low magnification (80× to 170×) and at high magnification (500× to 1900×). The coalesced bubbles were corrected to separate the bubble edges and obtain the most relevant numbers of bubbles within the melt [Proussevitch et al. 2007]. Area, number, and size information were quantified using `ImageJ` software. These values were used to calculate the crystallinity and vesicularity in the vesicle-free and crystal-free fractions. To achieve the proper stereological habit of vesicles in 3D projection (best-fit shape), the $\mathtt{CSD}_{\mathtt{slice}}$ spreadsheet developed by Morgan and Jerram [2006] was utilized. The best-

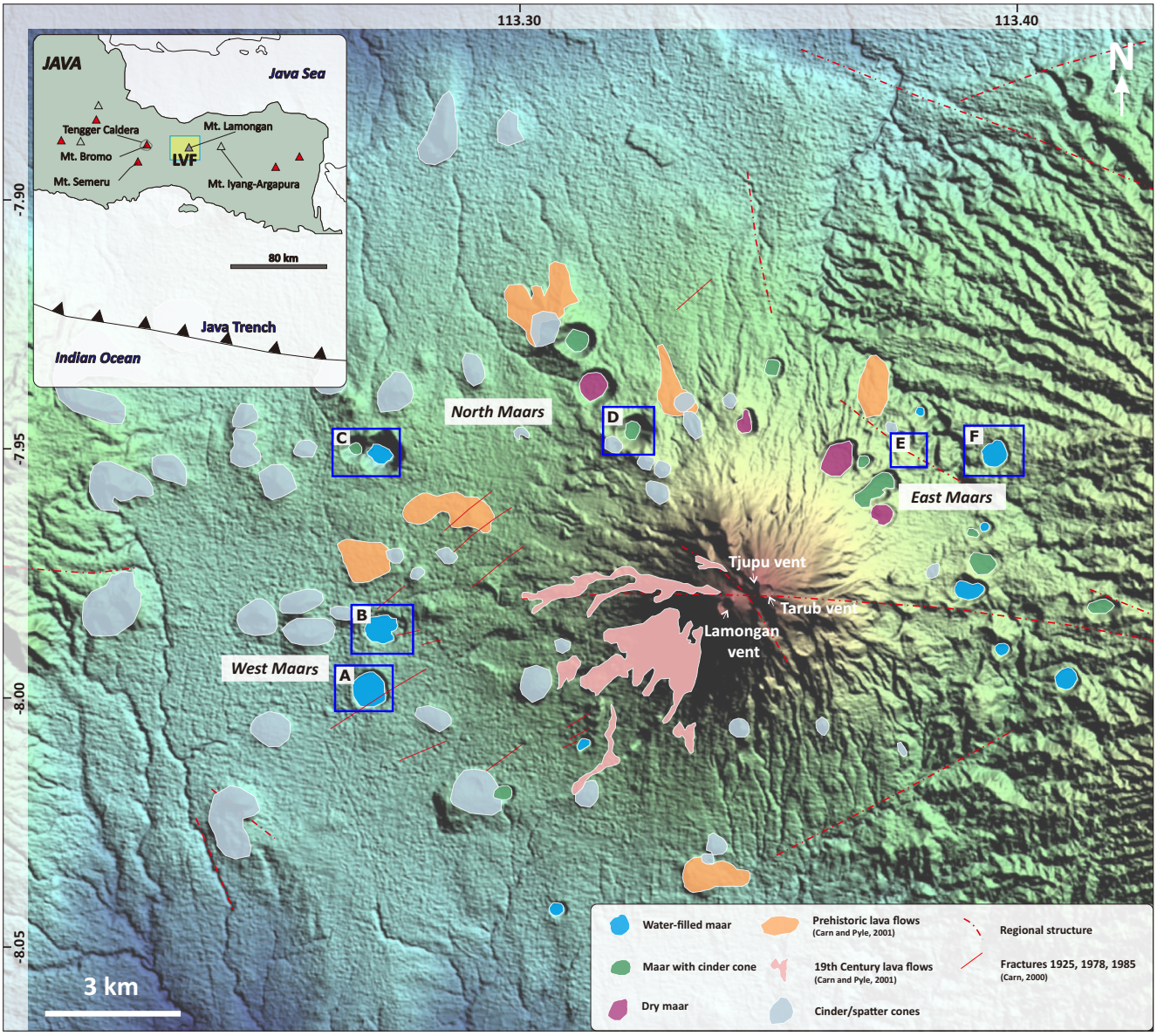

Figure 1: Location and sample map for the LVF maar complex. The digital elevation model (DEM) was downloaded from https://tanahair.indonesia.go.id/demnas. The maars included in this study are indicated by blue squares and labeled as follows: [A] Ranu Pakis, [B] Ranu Klakah, [C] Ranu Kering, [D] Ranu Air, [E] outcrop NE of Ranu Kembar, and [F] Ranu Segaran. The distribution of maars, lava flows, and cinder-spatter cones on LVF is based on Carn and Pyle [2001].

fit shape, represented by x-y-z values, was then input into the `CSDCorrection v.1.6` software developed by Higgins [2000, 2002] and Higgins and Chandrasekharam [2007] for quantification of the vesicle number densities (VND) and vesicle volumes (VV)*.

The geochemical composition of the eruption products from the LVF maar complex was determined through X-ray fluorescence (XRF) analysis. Initially, the freshest (glossy) and least altered particles from the 0.5–1 mm size fractions were hand-selected from representative ash classes. The ash grains were carefully selected based on their class from individual layers, ensuring there was no mixing with grains from different classes, layers, or other maars. These particles were further categorized into five classes (as further explained below), such as black non-vesicular (bnv), black vesicular (bv), grayish-black (gray) from east maars, clear-pale brown (cb + pb), and orange-brown (ob) ash particles. Enough ash particles of each class were combined to obtain sufficient mass for analysis (1.2–1.6 g). In addition, lava samples (from the north and east regions) and scoria cone deposits (from the north region) were also analyzed to identify geochemical variations in the area. The lava samples were collected from lava flow outcrops, while the scoria cone samples were obtained from lapilli fall deposits. All of the samples were crushed, pulverized, and prepared as glass beads (melting pellets) and analyzed for major oxides using a ZSX Primus II from Rigaku Co. at Akita University.

*http://www.uqac.ca/mhiggins/csdcorrections.html

As we did not have glass compositions (due to the high crystallinity groundmass on the ash particles), viscosities were estimated using whole rock compositions and PELE modeling coupled with constraints from the textural analysis. The determination of liquidus temperature and viscosity was obtained using PELE software*. This software was utilized by integrating the geochemistry data with the assumption of 1.5 % H_2O content, fO_2 at the QFM buffer, fractional crystallization, temperature from 1200–900 °C (increment = 4 °C), and pressure from 1000–10 bar (increment = 10 bar). The initial magma water content used for viscosity determination is referenced from Kelud volcano, as it possesses a similar magma composition to Lamongan volcano and is the only nearby volcano that provides this information. Cassidy et al. [2016] calculated the water content in Kelud volcano's magma under the assumption of dissolved H_2O within plagioclase-hosted melt inclusions. Subsequently, we matched PELE results with quantified crystallinity and observed mineral assemblages from the textural analysis. Then the temperature and viscosity values at equivalent crystallinities and mineral assemblages were taken as approximations of the natural magma conditions.

Furthermore, the relative viscosity of the samples was assessed by analyzing crystal content (crystallinity) and crystal size distributions (CSD) in vesicle-free fractions. The relative viscosity values were calculated using the Klein et al. [2018] spreadsheet, which incorporated the parameters of crystal aspect ratio and Feret diameter obtained from ImageJ together with the crystallinity data of each ash particle.

3 Results

3.1 The maar deposits

The LVF maar deposits can be categorized into three locality groups (Figure 1) based on proximity to the center of the Lamongan volcano and the type of crater, i.e. water-filled or dry. The three groups are [1] west maars (Ranu Pakis and Ranu Klakah); [2] north maars (Ranu Kering and Ranu Air); and [3] east maars (Ranu Segaran and an outcrop near Ranu Kembar). Water-filled craters characterize west and east maars, whereas north maars are distinguished by their dry craters (as described in Table 1).

Ranu Pakis Maar, a water-filled crater with a diameter of 750 m, comprises three outcrops on the eastern crater wall (~19 m total thickness). The lower layers comprise grayish-brown deposits with lapilli and blocks, with intermittent intercalations of thin ash layers bearing accretionary lapilli. The upper layers consist of grayish-brown consolidated fine ash to lapilli deposits with some intercalations of thin dark and pale-yellow layers (10 cm) (Figure 2B).

Ranu Klakah is a water-filled maar with a diameter of 675 m, exhibiting two outcrops with lateral continuity and a total exposed thickness of 6.3 m. The deposits are characterized by plane-parallel (planar) layers of fine to coarse ash from 10 to 15 cm in thickness. These layers are consolidated, well-sorted, and include a high proportion of accretionary lapilli. Within the lower layers, bomb sag structures resulting from the impact of ballistic materials on relatively soft and unconsolidated deposits can be observed (Figure 2C). The upper layers are pale yellow, while the lower layers exhibit a grayish-brown color (Figure 2D).

Ranu Kering is a dry crater maar with a diameter of 390 m, located on the eastern side of the water-filled crater of Ranu Bedali maar. The name "Ranu Kering" translates to "no water accumulation in the crater" in the local language. The western crater wall of Ranu Kering exhibits two pyroclastic outcrops with a 30 m elevation difference and a combined thickness of 10 m. The lower outcrop layers are grayish-brown, coarse (coarse ash to blocks), and contain abundant orange-brown scoria clasts 0.5–2 cm across (Figure 2E). Cross-lamination and bomb-sag structures are frequently observed at the base of the deposit. The upper outcrop displays grayish-black, coarse ash to lapilli with a high concentration of orange-brown scoria clasts and glassy black ash.

Ranu Air is a 350 m diameter dry crater maar and, of those in this study, is situated closest to Lamongan volcano's center. The total exposed thickness of pyroclastic deposits is 6 m. These deposits are characterized by a dark-greyish color, coarse ash to lapilli, loose to semi-consolidated, lithic-rich layers, and interlayering with accretionary lapilli-bearing ash layers (Figure 2F).

An outcrop measuring 1.2 m in thickness is located 200 m to the northeast of Ranu Kembar Maar. The pyroclastic deposits are composed of grayish-brown, severely weathered, unconsolidated, thinly laminated layers (15 cm) ranging in grain size from coarse ash to lapilli. The upper part of the deposits contains interlayered thin black ash (~4 cm thickness) (Figure 2G).

Ranu Segaran, a 545 m diameter water-filled maar, exhibits a strongly weathered, 1.8 m thick outcrop that was exposed by construction activities. The deposits are composed of grayish-orange fine ash to lapilli and contain cross-lamination structures (Figure 2H). The deposits are characterized by a high concentration of sparkling-black particles of opaque minerals.

We generalized the succession of the proximal maar ejecta ring deposits by comparing the vertical successions of all the outcrops found within LVF (Figure 2A). This generalized stratigraphic section is divided into three major units, distinguished by distinct characteristics.

Unit 1 comprises dark gray block-bearing lapilli layers with planar and cross-laminated bedding. These layers are clast-supported, poorly sorted, semi-consolidated, and commonly display the preserved impact structure of ballistic blocks. The lower bed is a lithic-rich layer with a significant block size (>20 cm), while the upper bed consists of lapilli-dominated deposits interlayered with lapilli-bearing coarse ash layers.

A bedded package with cross-lamination and plane-parallel lamination characterizes unit 2. The predominant lithofacies within this unit are creamy brown to dark gray coarse ash to lapilli, occasionally with blocks, exhibiting a moderate degree of sorting. This lithofacies is typically matrix-supported and exhibits a semi-consolidated character. Additionally, the unit contains minor interlayered accretionary lapilli-bearing ash layers. Unit 2 is present in most of the studied maars.

Unit 3 is characterized by planar laminated ash deposits, commonly interlayered with accretionary lapilli. The unit ex-

*https://nicholas.duke.edu/people/faculty/boudreau/DownLoads.html

Table 1: The relationship between ash particle distribution with the physical properties of LVF maars. VJ = juvenile volume; VE = ejecta volume; d_{max}/d_{min} is a measure of maar shape (1= circular, >1= increasingly ellipsoidal). Asterisks indicate information taken from Carn [2000].

Characteristics		West		North		East	
		Ranu Pakis	Ranu Klakah	Ranu Kering	Ranu Air	Outcrop NE Ranu Kembar	Ranu Segaran
ratio	bv/bnv	Low		Low		Very low	
	cb/pb	Moderate		Moderate		Low	
	cb+pb / bv+bnv	High		Moderate		Low	
ob		Rare		Rich	Rare	Rare	
fc		Rare		Rare	Moderate	Moderate	Rich
SiO_2 (average wt.%)		49.99	50.40	51.31	49.18	46.16	44.81
D_{mean}* (m)		755	675	395	350	-	545
Maar shape* (d_{max}/d_{min})		1.13	1.25	1.43	1.55	-	1.42
V_J* DRE ($\times 10^6$ m^3)		7.4	3.9	2.5	1.8	-	17
V_E* DRE ($\times 10^6$ m^3)		50	37	17.8	12.7	-	20
Maar type		Water-filled maars		Dry maars		Water-filled maars	

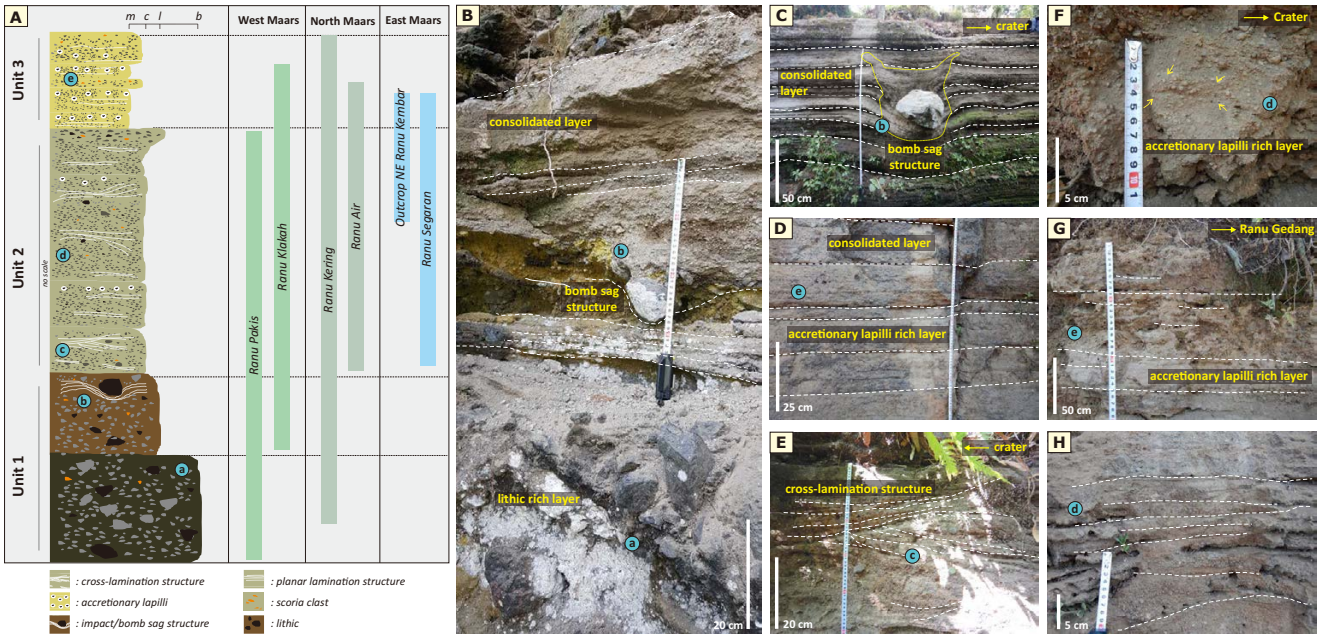

Figure 2: [A] Generalized stratigraphic succession of the LVF maar complex. Vertical bars indicate the existence of a preserved outcrop from each maar, which is compared to the generalized stratigraphy. Blue circles with the letters denote depositional features on the stratigraphy unit. Images from representative outcrops are shown for [B] Ranu Pakis, [C–D] Ranu Klakah, [E] Ranu Kering, [F] Ranu Air, [G] outcrop NE Ranu Kembar, and [H] Ranu Segaran.

hibits a yellow to dark gray color and comprises well-sorted fine to coarse ash displaying moderate consolidation.

3.2 Ash characteristics

3.2.1 *Ash types and morphology*

Based on the petrographic and scanning electron images, the ash particles have been categorized as juvenile particles or "other." There are two types of juveniles: type A and type B. Juvenile A grains are further subdivided into four classes: black non-vesicular, black vesicular, clear-brown, and pale-brown, which are described below. Juvenile B grains include only one class, orange-brown. Other particles include free crystals and altered (recycled) ash particles (as shown in Figure 3) [e.g. D'Oriano et al. 2011; 2014]. Generally, a range of ash particle types and classes are present in all maar deposits in varying proportions (Figure 4).

Black non-vesicular ash (bnv) particles are characterized by their blocky shapes and stepped microcrystalline surfaces. This class of ash constitutes the most abundant fragments in the LVF maar complex, accounting for 28 to 49 vol. %, with slightly lower abundances observed in Ranu Klakah (25 vol. %) and Ranu Segaran (17–23 vol. %).

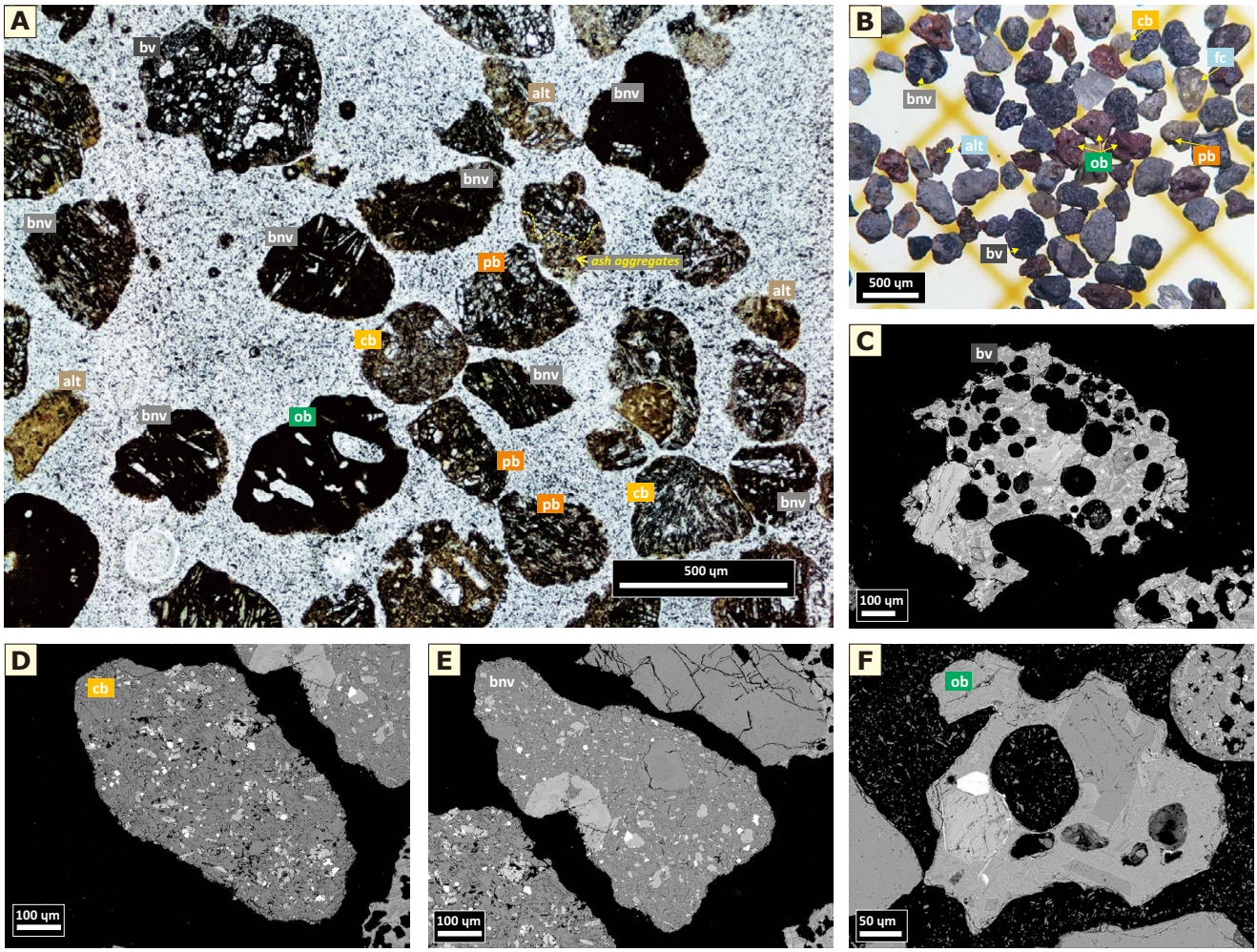

Figure 3: Representative images of ash particles from LVF maar complex, including [A] thin-section samples under plane-polarized light (PPL) mode, [B] ash particle grains under a binocular microscope, [C–F] backscattered electron (BSE) images of ash types ([C] bv ash, [D] cb ash, [E] bnv ash, and [F] ob ash). Ash particles can be categorized into three groups: juvenile A ash (cb, pb, bnv, and bv), juvenile B ash (ob), and other (fc and alt).

Black vesicular ash (bv) is an ash class with black-brown particles characterized by blocky to platy shapes and rough surfaces. The particles have equidimensional to elongate forms with convex outlines. While the bv ash particles are less abundant in the eastern maars (1.3–3.5 vol. %), they are slightly more common in the northern and western maars (4–10 vol. %).

Clear-brown (cb) and pale-brown (pb) particles are characterized by their sub-equant to elongate form, blocky to sub-round shape, rough surface, and microcrystalline texture. The average concentration of cb + pb ash particles decreases from 20.8 vol. % at the west maars to 12.4 vol. % at the north maars and to 6.3 vol. % at the east maars.

Orange-brown ash (ob) particles are characterized by an irregular to elongate shape with a smooth surface. Among the different classes of grains, the ob ash particles are the least abundant, accounting for 0.5–2.3 vol. %, except in the samples from Ranu Kering Maar, where they represent a higher proportion of 7–9 vol. %.

Free crystals (fc) range in size from 100 µm to 1 mm and can be either intact or broken crystals of plagioclase, pyroxene, olivine, hornblende, and opaque minerals. These crystals are derived from either magma or country rocks. The distribution of the fc particles gradually increases from the west maars (average: 3.3 vol. %) to the north maars (average: 12 vol. %) and further to the east maars (average: 31.8 vol. %). Among all the studied maars, samples from Ranu Segaran have the highest concentration of fc particles, with 50 vol. %.

Altered ash (alt) particles are small, dark-brown (about 200 µm) particles of weathered and altered ash. Except for the mag43-5 sample, which is an outcrop northeast of Ranu Kembar and has a distribution of 33 vol %, alt ash particles are relatively rare from LVF maar complex deposits, ranging from 2 to 14 vol %.

The ash components were initially defined through visual characterization during componentry analysis, after which quantitative morphology, texture, and geochemical analyses provided complementary datasets (explained below) that val-

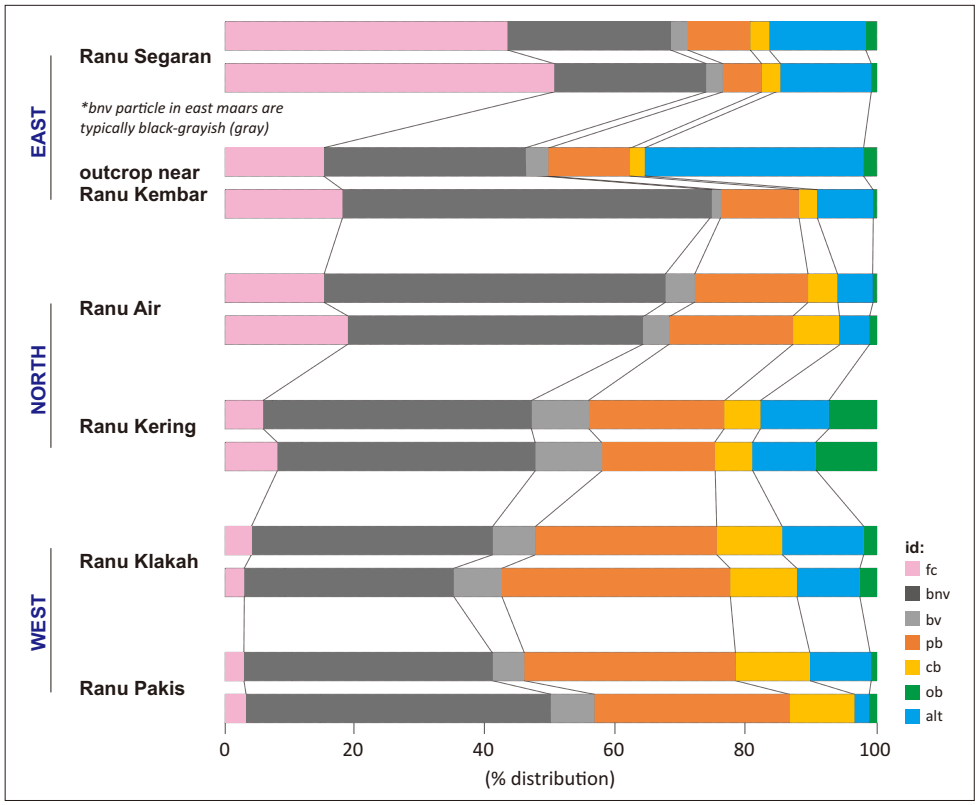

Figure 4: Componentry distribution of the 125–250 µm fraction from the LVF maar complex deposits. The spatial view shows a decreased ratio distribution of brown ash (cb + pb) and black ash (bv + bnv) from east-north-west maars, while the free crystal content shows a contrary positive trend.

idated and further described the characteristics of these visually defined juvenile types and classes.

3.2.2 *Particle shape*

Morphometric parameters were utilized to differentiate ash particle shapes based on various characteristics, including Axial Ratio, Solidity, Convexity, and Form Factor [Liu et al. 2015]. Axial Ratio was used to distinguish between compact and elongate shapes, while Solidity was used to measure the area-based complexity and roughness of the ash particles. Convexity was used to measure the perimeter-based complexity and roughness, and Form Factor was utilized to quantify the deviation of a particle from a circular shape. These morphometric parameters are commonly employed to characterize and distinguish between different types of ash particles.

The results of shape analysis (Figure 5; Table 2) suggest that the west and north maars ash particles possess high Solidity and Convexity values, with average values of 0.93 and 0.95, respectively, while the bv ash has slightly lower Convexity values (average 0.92). Additionally, the west and north maars ash particles have an average Axial Ratio and Form Factor of 0.70 and 0.68, respectively. Notably, the ob particles from the Ranu Kering (north maar) exhibit lower values of Solidity (average 0.74), Convexity (average 0.73), Axial Ratio (average 0.65), and Form Factor (average 0.32). In the eastern maars samples, the average Solidity and Convexity values were found to be 0.92 and 0.88, respectively, while the average Axial Ratio and Form Factor values were 0.73 and 0.59, respectively. On average, the juvenile A particles from the east maars had more complex outlines and less circular shapes than the north or west maar ash.

3.2.3 *Ash texture*

SEM images taken at 80× to 170× magnification reveal that all five classes of juvenile grains contain glass, crystals, and vesicles, but in variable proportions (Figure 6). Samples from the east maars were excluded from this investigation due to the substantial impact of the weathering process on their textural features. The degree of vesicularity was classified using the vesicularity index of Houghton and Wilson [1989]. Key vesicle properties such as vesicularity index, vesicle volume, and vesicle number density are summarized in Table 3. Vesicularity is the 2D area percentage of vesicles, while vesicle volume (VV) is the total 3D volume fraction estimated based on modeling vesicle size distributions.

1. bnv ash particles exhibit a non-to-poorly vesicular (average: 7.2 %) texture, and their average vesicle volume (VV) is 14.6 vol %. The grains are characterized by small vesicle sizes (long axis: average 57 µm), an average vesicle axial ratio of 0.60, irregular to elongate vesicle shapes, and irregular vesicle edges. These particles exhibit an average vesicle number density (VND) of 15.6×10^4 mm^{-3}. The particles have high crystallinity values ranging from 42 % to 58 %, with a mean value of 45.6 %. The crystals are 65 % plagioclase, 28 % pyroxene, 5.9 % Fe-Ti oxides, and 0.7 % olivine.

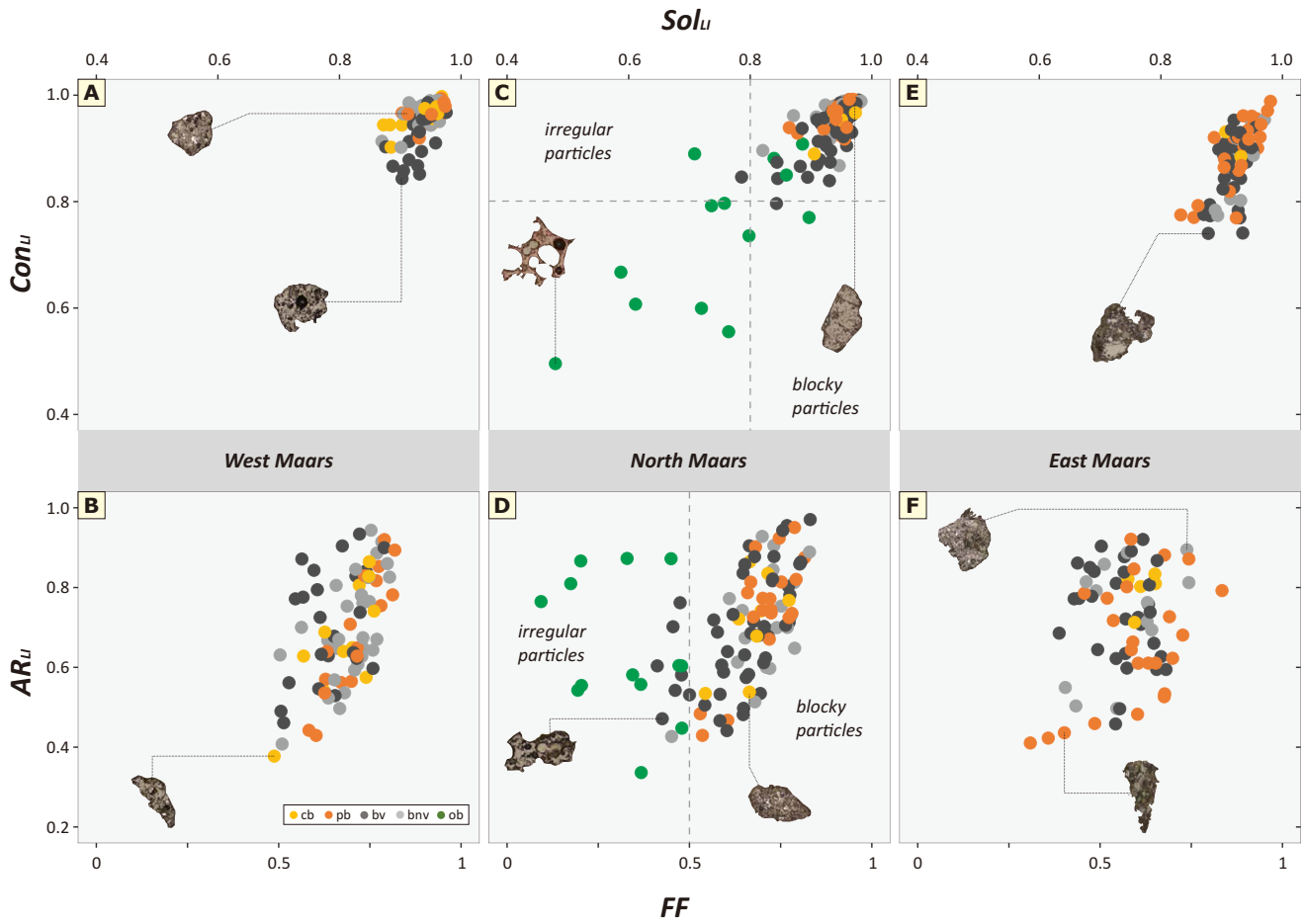

Figure 5: Conventional shape descriptors plot for juvenile ash particles from LVF, (top) Convexity vs. Solidity, and (bottom) Axial Ratio vs. Form Factor; for ([A] and [B]) west maars, ([C] and [D]) north maars, and ([E] and [F]) east maars. Distinct values are particularly shown by ob ash particles from north maars.

2. bv ash particles exhibit the highest degree of vesicularity (values ranging from 19 % to 33 %) among all investigated grains, with a mean VV of 40.7 vol. %. They show comparatively large vesicle sizes (long axis: average 130.8 µm), an average vesicle axial ratio of 0.63, and spherical to elongate vesicle shapes with coalesced vesicles. The smallest vesicles (less than 5 µm) are commonly distributed along the crystal edges. VND values range from 4 to 33 $\times$ 10^4 mm^{-3}. This class of particle has an average crystallinity of 31.5 %, with 75 % plagioclase, 16 % pyroxene, 8.7 % Fe-Ti oxides, and 5.3 % olivine.

3. cb and pb ash exhibit relatively low vesicularity, with average values of 20 % and 17 %, respectively. Both particle classes have a comparable average VV of 28.7 vol % and 24.7 % for cb and pb particles, respectively. These particles have a relatively large vesicle size (long axis: average 106.4 µm) with an average vesicle axial ratio of 0.58. The vesicles display irregular, amoeboid-to-elongate shapes and irregular edges. The cb particles exhibit a VND range of 3 $\times$ 10^4 mm^{-3} to 7 $\times$ 10^4 mm^{-3}, while the pb particles exhibit a VND range of 2 $\times$ 10^4 mm^{-3} to 24 $\times$ 10^4 mm^{-3}. The average crystallinity of these ash particles is 39.8 %, with plagioclase, pyroxene, Fe-Ti oxides, and olivine constituting 46 %, 38 %, 14 %, and 4.3 %, respectively.

4. ob ash is glassier than other ash classes (Figure 6). These grains consist of relatively low-vesicularity particles (average: 11 %) with an average VV value of 7.9 vol. %. They exhibit spherical to elongate vesicle shapes with a tendency for coalescence. The particles have the largest vesicle (long axis: average 147 µm) with an average vesicle axial ratio value of 0.66. The particles have low VND values ranging between 0.5 and 0.9 $\times$ 10^4 mm^{-3}. They display a low average crystallinity of 7.9 %, and the crystals consist predominantly of plagioclase (84 %) and Fe-Ti oxide (15 %) in the groundmass.

In addition to low-magnification texture analysis, we used high-magnification (500× to 1900×) backscattered electron imaging to obtain more detailed information on vesicularity and crystallinity. The results showed a wide range of vesicularity values for the different particle classes, with bv, bnv, cb, pb, and ob exhibiting average values of 39 %, 4.3 %, 8.3 %, 2.2 %, and 2 %, respectively. Furthermore, crystallinity measurements varied significantly among the particle classes, with bv, bnv, cb, pb, and ob displaying average values of 74 %, 68 %, 57 %, 46 %, and 27 %, respectively.

Table 2: Average values of morphometric parameters for ash particles from LVF.

Region	Maar	Ash class	CircDL	RecDL	ComDL	EloDL	FF	ARLI	ConLI	SolLI
West maars	Ranu Pakis	cb	1.22	0.9	0.72	1.91	0.67	0.64	0.95	0.93
		pb	1.2	0.9	0.76	2	0.7	0.65	0.97	0.95
		bv	1.29	0.95	0.73	1.94	0.61	0.68	0.91	0.92
		bnv	1.19	0.89	0.73	1.75	0.71	0.73	0.97	0.94
	Ranu Klakah	cb	1.23	0.91	0.74	1.95	0.67	0.7	0.96	0.92
		pb	1.17	0.9	0.77	1.65	0.73	0.73	0.96	0.95
		bv	1.23	0.92	0.73	1.81	0.67	0.74	0.94	0.94
		bnv	1.22	0.9	0.74	1.97	0.68	0.67	0.97	0.94
North maars	Ranu Kering	cb	1.22	0.92	0.74	1.59	0.68	0.79	0.95	0.94
		pb	1.22	0.9	0.73	1.99	0.69	0.72	0.96	0.94
		bv	1.28	0.95	0.74	1.84	0.63	0.71	0.92	0.92
		bnv	1.21	0.9	0.73	1.73	0.7	0.73	0.96	0.93
		ob	1.92	1.23	0.57	2.06	0.32	0.65	0.73	0.74
	Ranu Air	cb	1.23	0.91	0.73	2.01	0.67	0.63	0.94	0.94
		pb	1.18	0.9	0.76	1.57	0.72	0.77	0.96	0.95
		bv	1.24	0.92	0.74	1.93	0.66	0.68	0.94	0.94
		bnv	1.18	0.89	0.77	1.92	0.73	0.66	0.97	0.96
East maars	Outcrop NE Ranu Kembar	cb	1.28	0.97	0.74	1.48	0.61	0.81	0.88	0.93
		pb	1.37	1	0.71	2.07	0.55	0.65	0.88	0.92
		bv	1.35	1.01	0.72	1.65	0.55	0.77	0.85	0.91
		bnv	1.32	1	0.74	1.64	0.58	0.77	0.87	0.92
	Ranu Segaran	cb	1.27	0.96	0.73	1.59	0.62	0.77	0.91	0.92
		pb	1.27	0.95	0.74	1.9	0.64	0.67	0.92	0.94
		bv	1.33	0.97	0.71	1.93	0.58	0.68	0.89	0.92
		bnv	1.37	1.02	0.74	1.81	0.55	0.69	0.85	0.93

3.2.4 *Geochemical composition and rheological variation*

The analyzed volcanic ash particles from the LVF maar complex exhibit chemical compositions that span a range from picro-basalt to basaltic andesite (41.4–52.9 wt.% SiO_2 and 0.25–1.63 wt.% K_2O; Figure 7A). They are classified as low- to medium-K basalt with high MgO (cb + pb ash), medium-K picrobasalt to basalt with high MgO (grayish-black ash from east maars), and medium- to high-K basalt to basaltic andesite with moderate to low MgO content (bv + bnv and ob ash), respectively. Each ash class also has a different FeO* (iron total) concentration, gray, cb-pb, bv, and some portions of bnv ash show a relatively decreasing trend towards increasing silica; however, bnv and ob particles show indications of a relatively flat iron trend towards increasing silica concentration. In addition, the lava fragment samples (north and east lava) are classified as medium- to high-K basalt to basaltic-andesite, while the north scoria cone deposits are medium-K picrobasalt with the lowest SiO_2 (41.4 wt.%).

In stratigraphy, we infer the typical composition of various stratigraphic layers based on the bulk composition of different particle types. As evidenced by their silica concentrations, the geochemical composition of ash classes is relatively stable over time, as shown in Figure 8. The brown (cb + pb) ash particles exhibit low SiO_2, averaging 47.6 wt.% for the west maars and 46.2 wt.% for the north maars. The black ash (bv + bnv) displays an average silica content of 50.5 wt.% for the west maars and 49.7 wt.% for the north maars. In contrast, the orange ash (ob) demonstrates the highest average silica concentration, with 51.5 wt.% for the west maars and 53.2 wt.% for the north maars. Lastly, the grayish-black ash particles obtained from the east maar are characterized by the lowest average SiO_2, which stands at 45.8 wt.%.

Through the utilization of estimates based on observed bulk crystallinity and mineral assemblages, we were able to estimate the eruptive temperature and calculate melt viscosities for the ash particles. Moreover, by taking the observed porosity into account, the bulk rheological properties can be constrained (Table 4). The black particles (bv + bnv + bnv-m) from the west and north maars represent average values of silica concentration of 50.7 wt.%. They have corresponding average viscosities and liquid temperatures of $10^{3.58}$ Pa.s (~3800 Pa.s) and 1042 °C, respectively. The pale-clear brown ash particles (pb + cb) exhibit lower average values of silica at 46.8 wt.%. They have a lower average viscosity at $10^{2.76}$ Pa.s (~575 Pa.s) and a higher average liquid temperature at 1067 °C. Lastly, the ob ash particles displayed the highest silica content (average: 52.6 wt.%). These particles also have the highest liquid temperature (average: 1106 °C) and lowest viscosity (average: $10^{2.48}$ Pa.s or about 300 Pa.s).

Moreover, we applied crystal content and crystal size distribution to calculate the relative viscosities of ash particles

Table 3: The summary of vesicle properties within each class from LVF maar complex. All measurement results in this table are micrometers scale. *AR* means axial ratio.

Ash Type	Sample	Long axis	Short axis	Avg. long axis	Length	Width	Avg. length	Mean AR	Median AR	Vesicle type	Vesicle images
Clear-brown (cb)	1-3 cb	139.4	5	20.2	45.9	3.9	10.4	0.57	0.57	Irregular, amoeboid to elongate shapes, coalescence, irregular edges	
	5-12a cb	99.2	5	19.8	43.1	3.8	9.5	0.54	0.53		
	13-2 cb	88	4.8	17.1	61	3.9	9.6	0.61	0.63		
Pale-brown (pb)	1-3 pb	173.3	5.2	23.9	94.8	3.8	12.6	0.6	0.6		
	5-12a pb	91.2	5.2	20.4	54.4	4.3	10.5	0.57	0.57		
	13-2 pb	76.2	3.8	10	28.5	3.2	5.5	0.61	0.63		
	20-1 pb	77.5	3.5	9.4	42.7	2.9	4.9	0.58	0.58		
Black vesicular (bv)	1-3 bv	189	3.3	14.7	110.4	2.3	8.7	0.63	0.63	Spherical to elongate shapes, coalescence	
	5-12a bv	130.2	3.1	15.2	86.6	1.7	8.6	0.6	0.59		
	13-2-bv	111.5	5.4	19.9	70.8	4	11.7	0.63	0.64		
	20-1 bv	92.7	2.6	12.1	73.1	1.8	7.2	0.64	0.65		
Black non-vesicular (bnv)	1-3 bnv	71.5	3.5	11.4	34	3	6.1	0.62	0.61	Irregular to elongate shapes, irregular edges	
	5-12a bnv	33.8	2.1	6.1	16.8	1.7	3	0.58	0.57		
	13-2 bnv	36.9	2.7	8.1	17.9	2.2	4.7	0.63	0.63		
	20-1 bnv	49.1	2.8	8.4	16	2.4	4.3	0.58	0.59		
	20-1 bnv	93.5	4.1	13.2	38.8	3.2	7.1	0.61	0.61		
Orange-brown (ob)	1-3 ob	151.7	5.5	32.3	81.1	4.5	18.3	0.58	0.58	Spherical shapes, coalescence	

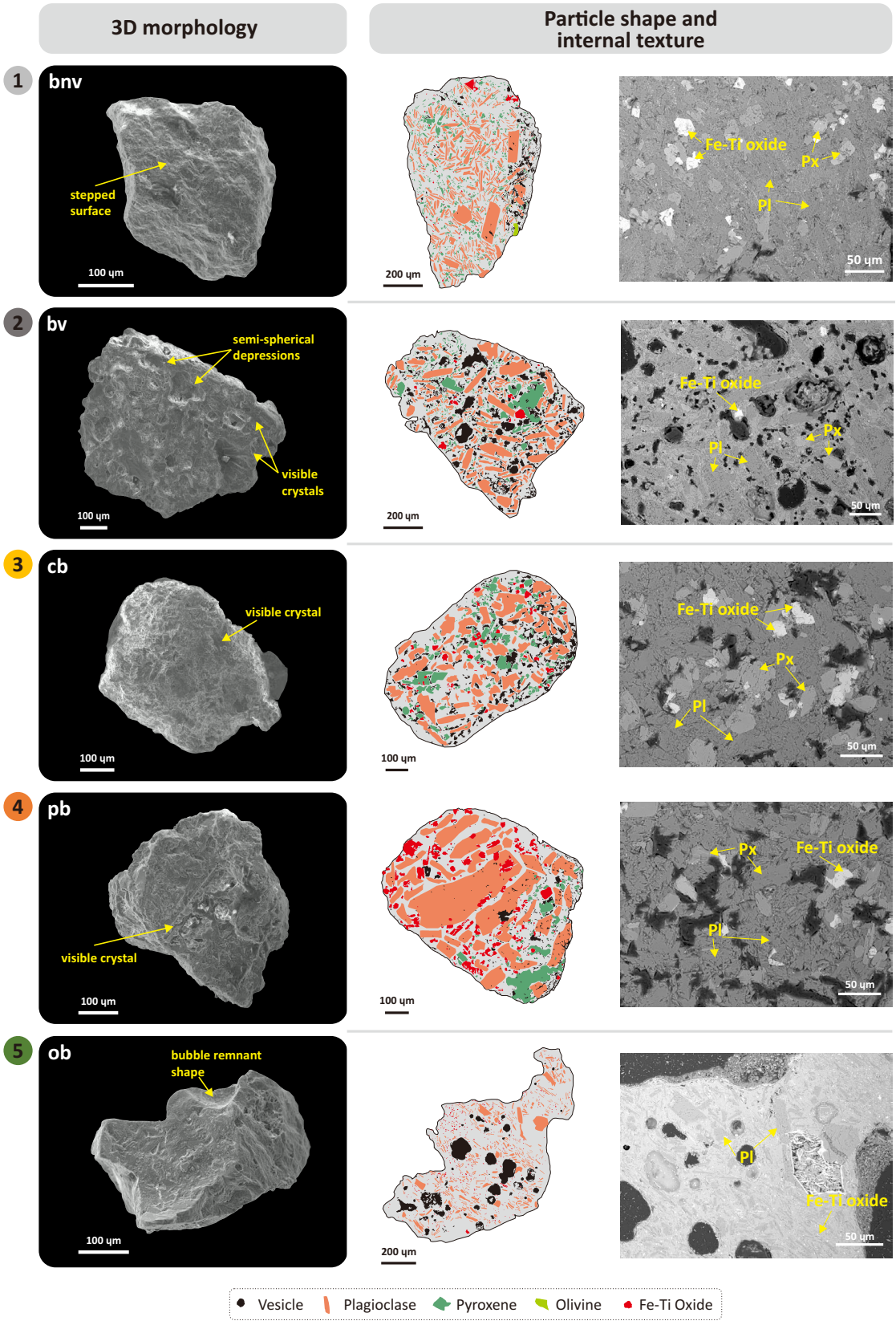

Figure 6: Micro-texture description for juvenile ash classes, including 3D morphology and representative digitized grain backscattered electron (BSE) images with textural features in high magnification (square images) from ash particles in LVF maar complex. The digitized BSE images were used for vesicular and crystal features calculations.

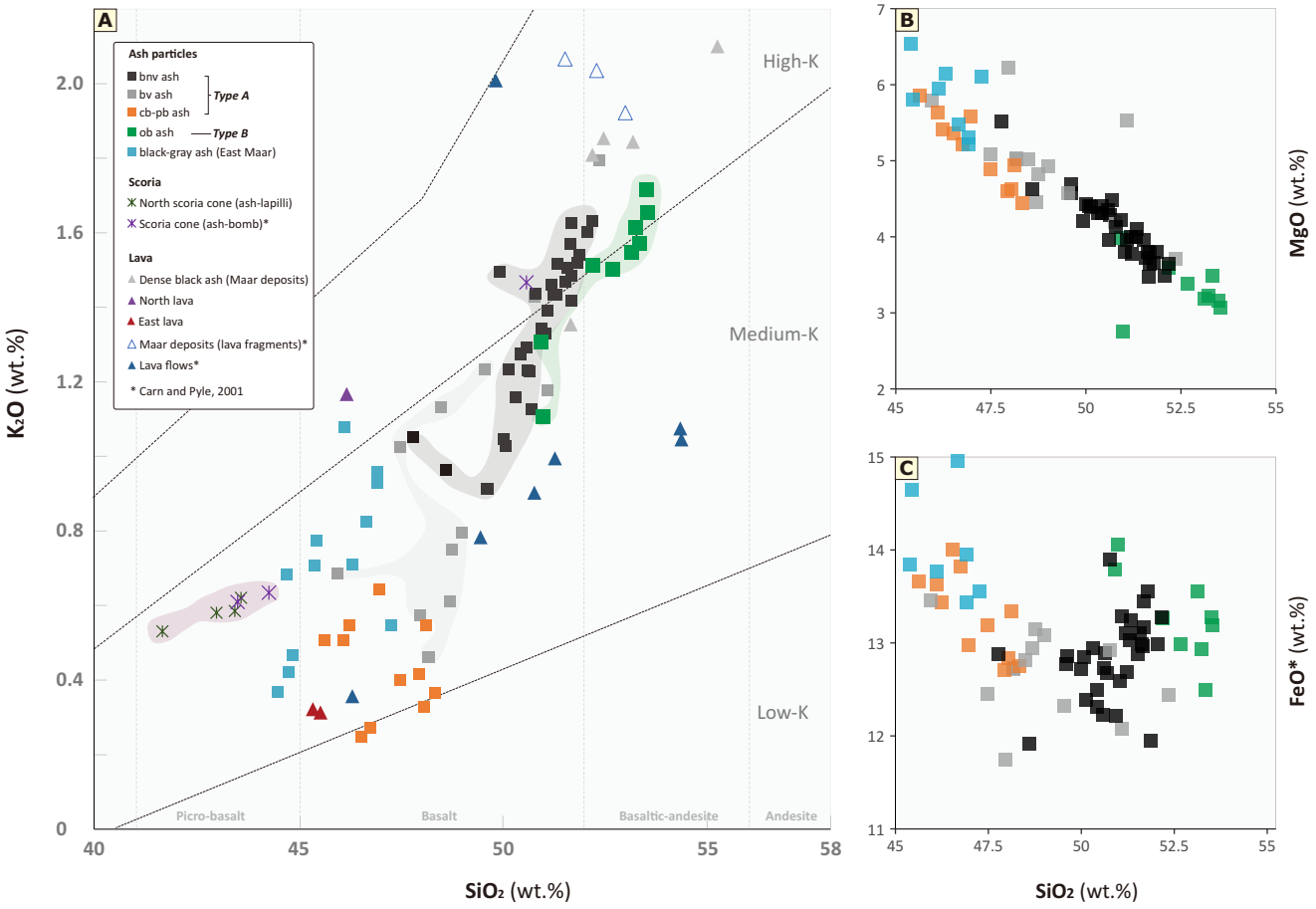

Figure 7: [A] Binary plot of K_2O (wt.%) vs SiO_2 (wt.%) for volcanic products in LVF, including volcanic ash from maar deposits, scoria fall deposits, and lavas. The rock series boundary lines are based on Ewart_1982 and Le_Maitre_1989. Binary plots of [B] MgO (wt.%) vs SiO_2 (wt.%) and [C] FeO* (wt.%) vs SiO_2 (wt.%). All the major element compositions presented have been normalized to 100 % volatile-free.

derived from the LVF maar complex. The analysis solely focused on the influence of crystal size on the rheology of the magmatic system without considering the contribution of vesicles [Klein et al. 2018], as done in previous studies of natural samples [e.g. Bagdassarov and Dingwell 1992]. As shown in Figure 9, each ash particle class exhibits a distinct trend in terms of crystallinity and relative viscosity. In general, the average values of relative viscosity show an increasing trend for ob, pb, bv, cb, and bnv ash particles. The ob particles exhibit the lowest average value of relative viscosity (1.1), while the bnv grains display the highest relative viscosity (average: 87.5).

4 Discussion

The observed vertical stratigraphic successions and variations across the LVF maar locations provide insights into the eruption processes and progression within this maar complex. The lower lithic-rich units containing large meter-scale blocks likely represent the initial explosive vent-opening phase (Figure 2B) [e.g. Lorenz 1986; Lorenz et al. 2017; Saucedo et al. 2017]. The coarse-grained units containing bomb sags may reflect the unsteady explosive eruption (Figure 2C). Progressing upwards, cross-laminated lapilli beds indicate deposition from pyroclastic surges, pointing to oscillations in intensity (Figure 2E). These coarser layers grade into the overlying finer-grained units, marked by extensive accretionary lapilli-bearing ash beds (Figure 2D, F–H). The fine ash and aggregation feature sustained eruption activities from prolonged magma-water interaction during crater development. This matches documented sequences of other maar eruptions globally [e.g. Lorenz 1986; White and Ross 2011; Jordan 2013].

The LVF maar ash particles were divided into two distinct types based on their characteristics, namely juvenile A (comprising black vesicular [bv], black non-vesicular [bnv], clear-brown [cb], and pale-brown [pb] classes) and juvenile B (consisting of orange-brown [ob]) ash particles. Free-crystal (fc) and altered (alt) ash particles were excluded from the analysis since they may not directly reflect primary magma fragmentation dynamics. However, their abundance within deposits is still characterized. This classification allowed the identification of the two end-members with contrasting properties, including differences in morphology, texture, composition, and rheological characteristics. Specifically, juvenile A ash particles exhibit a commonly blocky shape, high crystallinity, low vesicularity (with small vesicles), lower silica content, and higher viscosity. On the other hand, juvenile B ash particles

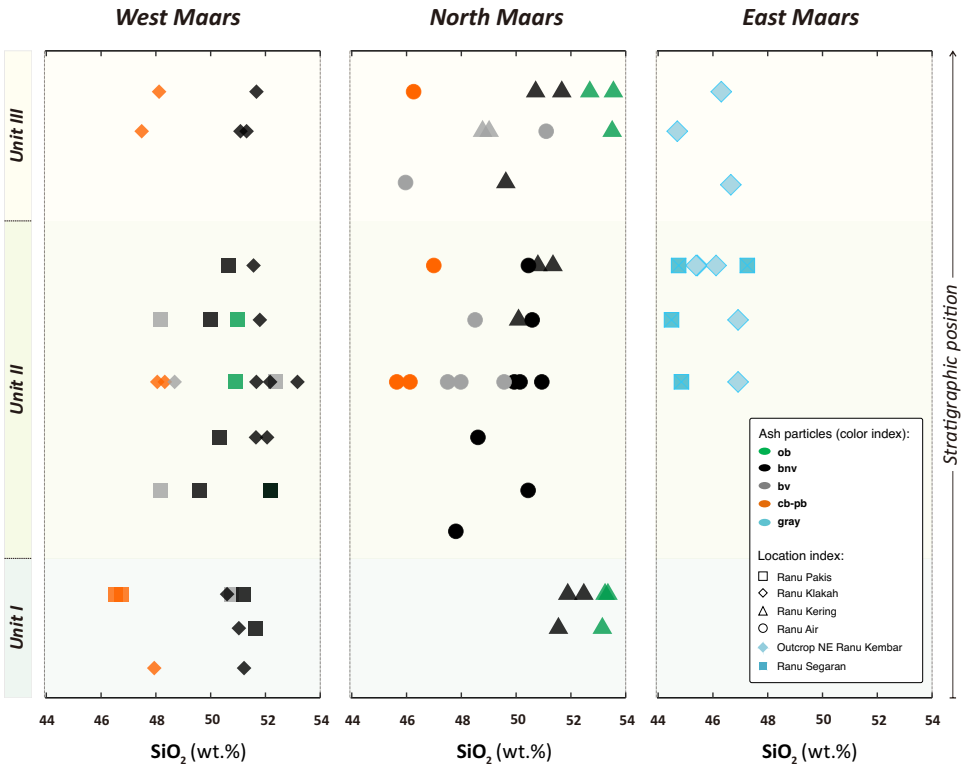

Figure 8: Temporal variation diagrams of SiO_2 (wt.%) content within a single eruption center of LVF maar complex.

are irregular in shape and have low crystallinity, low vesicularity (with bigger vesicles), higher silica content, and lower viscosity. We propose below that this reflects a different fragmentation process or eruption style for type A versus type B particles.

4.1 Textural variation of ash particles; ash formation

The ash particles produced by the LVF maar complex eruptions exhibit a diverse range of morphological and textural features. As depicted in Figure 10 and Table 4, juvenile A particles (bnv, bv, cb, and pb) exhibit more complex textural features compared to juvenile B ash particles (ob). The bnv ash particles have low vesicularity and crystal-rich groundmasses with tiny irregular vesicles. The complex vesicle shapes are considered to be influenced by the presence of crystals. The bv ash particles have slightly lower crystallinity, higher vesicularity, and higher vesicle density. The vesicles in these grains predominantly display a spherical to elongate shape, reflecting vesicle nucleation, growth, and coalescence processes. The cb and pb ash particles, having lower vesicle number densities and irregular bubble shapes, share similar textural properties with low vesicularity and crystalline tachylitic groundmass ash particles described by Murtagh and White [2013], who interpreted them as resulting from trapped volatiles within crystal networks. In contrast, the juvenile B ash particles (ob) have a less vesicular and less crystalline occurrence than the juvenile A particles, with a glassier groundmass. They have an unimodal vesicle distribution, indicating a trend of multiple stages of vesicle nucleation, growth, and coalescence [Shea et al. 2010]. These particles are thought to be the result of the rapid cooling of magma, which produced abundant microlites of plagioclase and Fe-Ti oxide.

The explosive eruption induced by magma-water interaction (phreatomagmatic eruption) is commonly regarded as the primary factor for ash formation at maar volcanoes, where magma fragmentation implies rapid quenching and water vaporization [Wohletz and Sheridan 1983; Németh 2010; White and Valentine 2016]. Based on field observation, pyroclastic deposits, and details of ash particles derived from the LVF maar complex, we infer that this process indeed played a significant role. The deposits are characterized by a high proportion of fine fragments, cross-bedding, bomb sags, and accretionary lapilli. Many ash particles exhibit blocky and equant shapes as the product of brittle fragmentation due to intense magma-water explosions. However, at Ranu Kering (north maars), ash products often display fluidal-like orange particles (constituting over 10 % of the component), suggesting ductile (magmatic) fragmentation for those grains.

Magma that is rich in crystals can undergo brittle fragmentation during rapid deformation [Németh 2010; Miwa et al. 2013]. Blocky morphologies are easier to recognize when dealing with dense (low vesicularity) magma [Heiken and Wohletz 1985]. However, even hot magma with poor crystallinity and low viscosity can undergo brittle fragmentation under intense deformation and rapid cooling during phreatomagmatic eruptions [Zimanowski et al. 1991].

Juvenile A particles exhibit a compact distribution of particle shapes, especially on the Solidity-Convexity diagram (Figure 5A, C, E). These phreatomagmatic particles are mostly dense, with few perimeter concavities, resulting in high values of Convexity and Solidity (> 0.8). Type B particles (class ob),

Table 4: Summary of vesicle features, bulk crystallinity, and crystal fraction distribution of ash classes from the LVF maar complex. *n* = number of vesicles; VND = vesicle number density (× 10^4 mm^{-3}); BV% = bulk vesicularity [high magnification]; VV% = vesicle volume; Av. VV% = average vesicle volume; Cry % = bulk crystallinity [high magnification]; Pyroxene (Px); Plagioclase (Pl); Fe-Ti oxides mineral (Fe-Ti); Olivine (Ol); SiO_2 = average silica content. The estimated liquid temperature (T) and log viscosity variations (log*F*) of LVF maar complex magma are referred from the geochemical composition of the ash particle types. They were calculated using PELE software with the assumption of 1.5 % H_2O content, fO_2 at the QFM buffer, and fractional crystallization condition. The temperature and viscosity were obtained from crystallinity and mineral assemblages that were similar to those in the PELE calculation and textural analysis result. η*r* = relative viscosity.

Ash type	Sample	Vesicle features					Cry %	Crystal Fraction %				ηr	*T* (°C)	log*F* (Pa.s)	Avg. SiO_2 (wt%)
		n	VND	BV%	VV%	Av. VV%		Px	Pl	Fe-Ti	Ol				
bv	1-3 bv4	819	11.5	27 [31.5]	44.4	40.7	40 [78.4]	11.2	83.9	3.8	1.1	9.7	1076	2.75	50.7
	5-12a bv2	560	11.9	28	41.5		43	25	72.1	2.8	-	14.9	1048	2.53	
	13-2 bv3	366	4.16	19 [48.1]	28.9		18 [69.9]	14.2	52.3	23.9	9.5	2.1	1093	2.89	
	20-1 bv3	925	33	33	47.9		25	-	95.5	4.3	-	3.1	1069	3.34	
bnv	1-3 bnv-m3	252	9.26	8 [2.5]	14.8	12.3	42 [66.9]	25.6	69.6	4	0.7	11.1	1060	3.47	
	5-12 bnv-m2	156	24	3	6.4		49	35.9	57	7	-	19.3	979	4.86	
	13-2 bnv-m1	506	21.1	6 [4.8]	9.3		40 [69.6]	17.9	72.3	9.8	-	8.2	1039	3.83	
	20-1 bnv-m1	-	-	-	-		58	13.3	84.4	2.2	-	386.3	951	5.24	
	20-1 bnv1	261	8.07	11	18.8		39	49.9	43.3	6.8	-	7	1063	3.32	
cb	1-3 cb2	280	3.87	18	28.4	28.7	27	68.2	19.8	12	-	3.1	1114	1.93	46.8
	5-12a cb1	271	7.02	22	32.3		50	25.7	67.9	6.4	-	25.3	1038	3.63	
	13-2 cb4	272	4.62	16 [3.6]	25.5		55 [57.1]	22.7	69.4	7.9	-	86.3	-	-	
pb	1-3 pb2	189	2.56	24	45.6	24.7	26	55.7	28.5	15.8	-	3	1105	1.33	
	5-12a pb1	258	3.81	17	25.3		27	52	17.9	30.1	-	3.2	1084	2.57	
	13-2 pb1	352	10.6	5 [1.8]	9.2		31 [47.6]	35.7	46.4	13.6	4.3	4	-	-	
	20-1 pb1	421	24.4	11	18.6		63	10	74.8	15.2	-	-	995	4.37	
ob	1-3 ob2	60	0.92	19	20.2	17.3	0.3	-	100	-	-	1.1	1138	1.68	52.6
	13-2 ob5	57	0.55	3 [2]	14.4		15 [27.8]	-	84.2	15.8	-	1.8	1074	3.29	

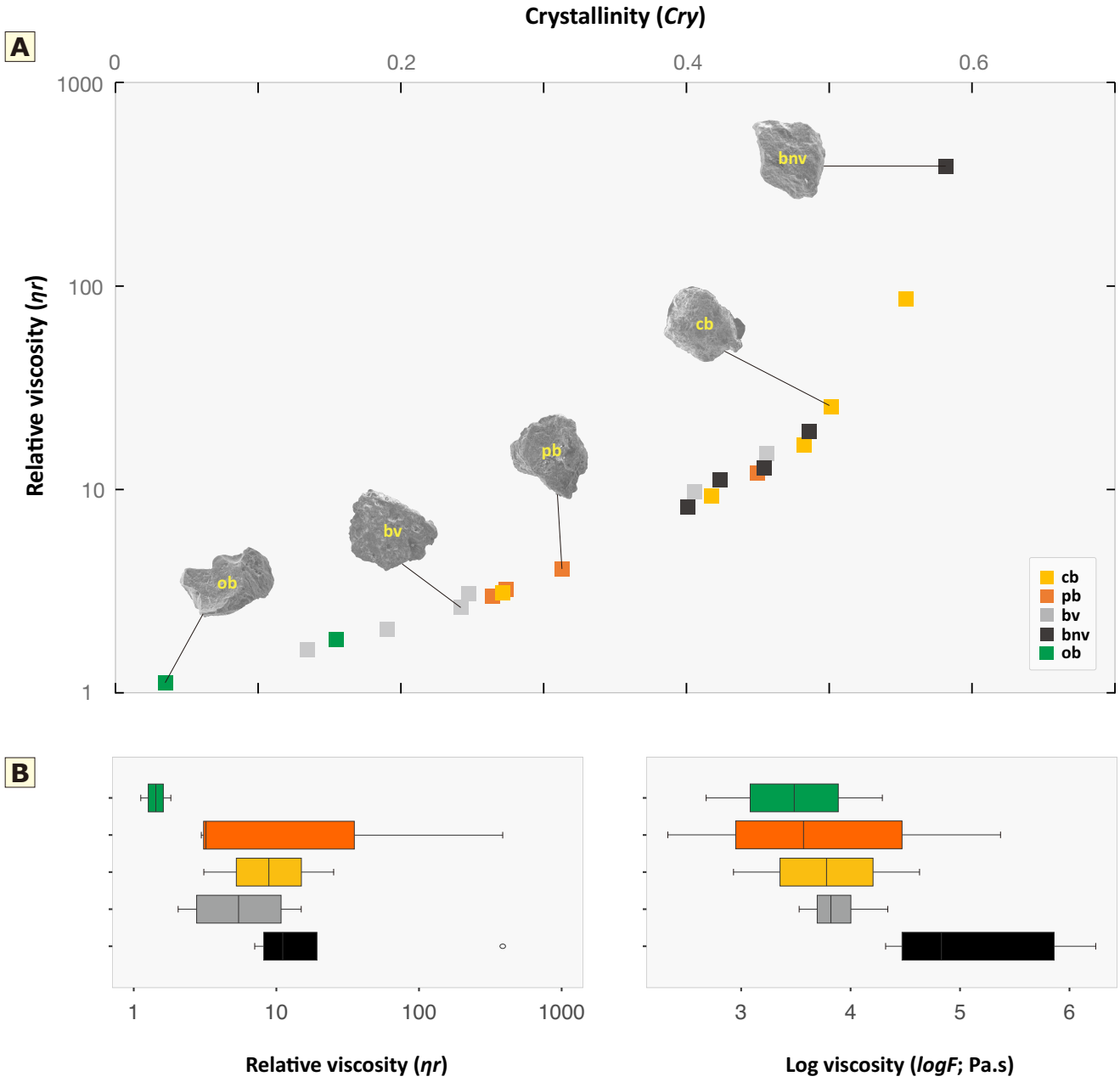

Figure 9: [A] Plot of relative viscosity vs. crystallinity of ash particles from the LVF maar complex. Results show an increasing exponential trend from low ratio values of ob ash, bv ash, and pb-cb ash, to high ratio values of bnv ash. [B] Comparison of the trend between relative viscosity and log viscosity of each type of ash particle. Both show a negative trend from orange (ob), brown (pb + cb), to black (bv + bnv) ash particles.

interpreted as magmatic, have more vesicles visible on their margins and therefore have lower Convexity and Solidity values (< 0.8). They also have a lower Form Factor value, with a transition at 0.5 (dashed vertical line, Figure 5D). In detail, there is a minor overlap between types A and B, potentially indicating transitional features in a few grains. Within the overall regions, juvenile A particles are slightly more blocky, with higher Convexity and Solidity values, while juvenile B particles from the north maars are slightly more irregular, with lower values for both parameters.

We utilized hierarchical clustering analysis (Figure 11) to investigate the particle shapes of volcanic deposits from the LVF maar complex using both image particle analysis (IPA) parameters [Dellino and Volpe 1996] and the shape parameters of Liu et al. [2015]. The parameters used were Circularity, Rectangularity, Compactness, Elongation, Form Factor, Axial Ratio, Convexity, and Solidity. The clustering referred to the degree of similarity using the Euclidean distance scale (height) [e.g. Maria and Carey 2002; 2007; Jordan et al. 2014; Liu et al. 2015; Dürig et al. 2021]. Three clusters of particles are distinguished using this procedure: [1] blocky and equant shapes

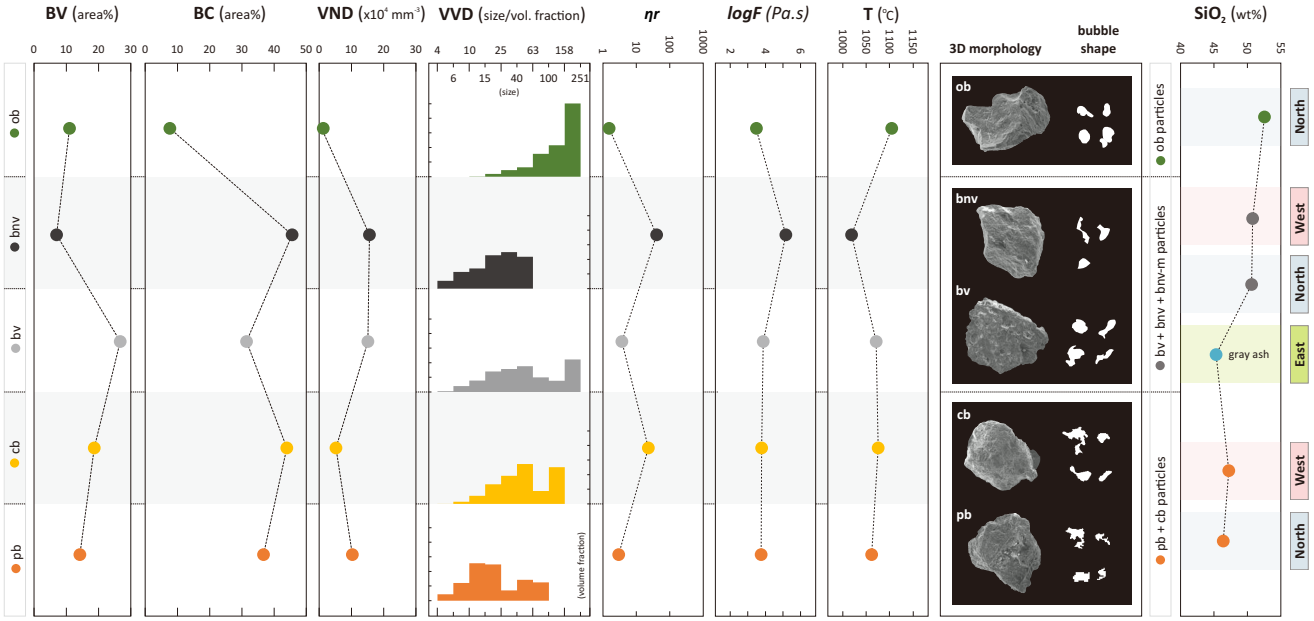

Figure 10: Summary of textural features and morphology of ash particles from the LVF maar complex with their corresponding rheological variations. The variables presented are average values from representative ash particle types, including BV (bulk vesicularity), BC (bulk crystallinity), VND (vesicle number density), VVD (vesicle volume distribution), η*r* (relative viscosities), log*F* (log viscosities), T (liquid/magma temperature), SiO_2 (silica content).

with smooth (1a) and rough (1b) outlines; [2] blocky to planar, sub-equant to elongate shapes with rough outlines; and [3] irregular shapes with rugged outlines. There is no general correlation between these shape clusters (1a, 1b, 2, and 3) and the particle types defined during componentry (types A and B, with type A subdivided into four classes), as the clusters are based solely on shapes, whereas the componentry types and classes integrate colors, internal textures, etc. However, some trends can be noted. Shape cluster 3 consists only of type B (class ob) particles; in these grains, large vesicles (vesicle remnant shape) create a distinct cluster of irregular shapes with rugged outlines. We interpret that the ob particles, especially those in cluster 3, were formed by magmatic fragmentation. Type B (class ob) grains also appear in shape cluster 2, along with some more irregular and elongate type A grains; in short, cluster 2 has transitional properties between irregular and blocky shapes. Finally, shape clusters 1a and 1b consist almost entirely of type A particles with mostly blocky shapes, which are interpreted as brittle products related to phreatomagmatic fragmentation. Within type A particles, 84 % are in shape clusters 1a and 1b (with mostly block shapes), and 16 % are in shape cluster 2 (with sub-equant shapes). Within juvenile B particles, 54 % are in shape cluster 2, and 36 % are in shape cluster 3. Our results are consistent with previous studies that have shown that a single eruption can produce a wide range of particle morphologies [e.g. Sheridan and Wohletz 1983; Wohletz and Sheridan 1983; Dellino and Liotino 2002; Mattsson 2010]. Even though the characteristics are different, the ash particles from the LVF maar complex show a clear distribution of the most common shapes (clusters 1a, 1b, and 2). The clustering analysis method we employed is more effective in identifying different particle shapes than binary diagrams, and can be applied to other volcanic deposits to further our understanding of the eruption mechanisms and processes.

4.2 Integration of textural features and geochemical compositions

Klein et al. [2018] determined the rheological properties of natural mafic to intermediate samples by analyzing the crystal-size distribution of vesicle-free magma. The results showed that samples with low crystallinity would have lower relative viscosity and vice versa (see Fig. 3d in Klein et al. [2018]; Mader et al. [2013]). In general, each class of ash particles in the LVF maar complex has its range of crystallinity. The crystallinity relatively increases from orange to black to brown ash, which is also how their relative viscosities change (Figure 9). More specifically, we investigated the implications and relationship of relative viscosity (η*r*) and bulk viscosity (log *F*) to ash particle shape and morphology. As shown in Figure 9A and 9B, both relative and bulk viscosities have similar decreasing values from bnv to cb to ob particles. The relatively higher viscosity of blocky juvenile A (bv + bnv + cp + pb) particles compared to juvenile B (ob) particles indicates a more active crystallization process. However, the bv particles, which contain lower silica content and have a lower crystallinity than bnv particles, have a slightly lower viscosity. Despite their long-range viscosities and relatively low silica content, the brown particles (cb + pb) display morphological similarities in the form of blocky to sub-round shapes, as shown in the shape distribution ratio in Figure 11. All four classes of type A particles (bv, bnv, cp, and pb) are evenly represented in shape cluster 1, which has the blockiest shape. These observations suggest that within phreatomagmatic eruptions, magma parcels with

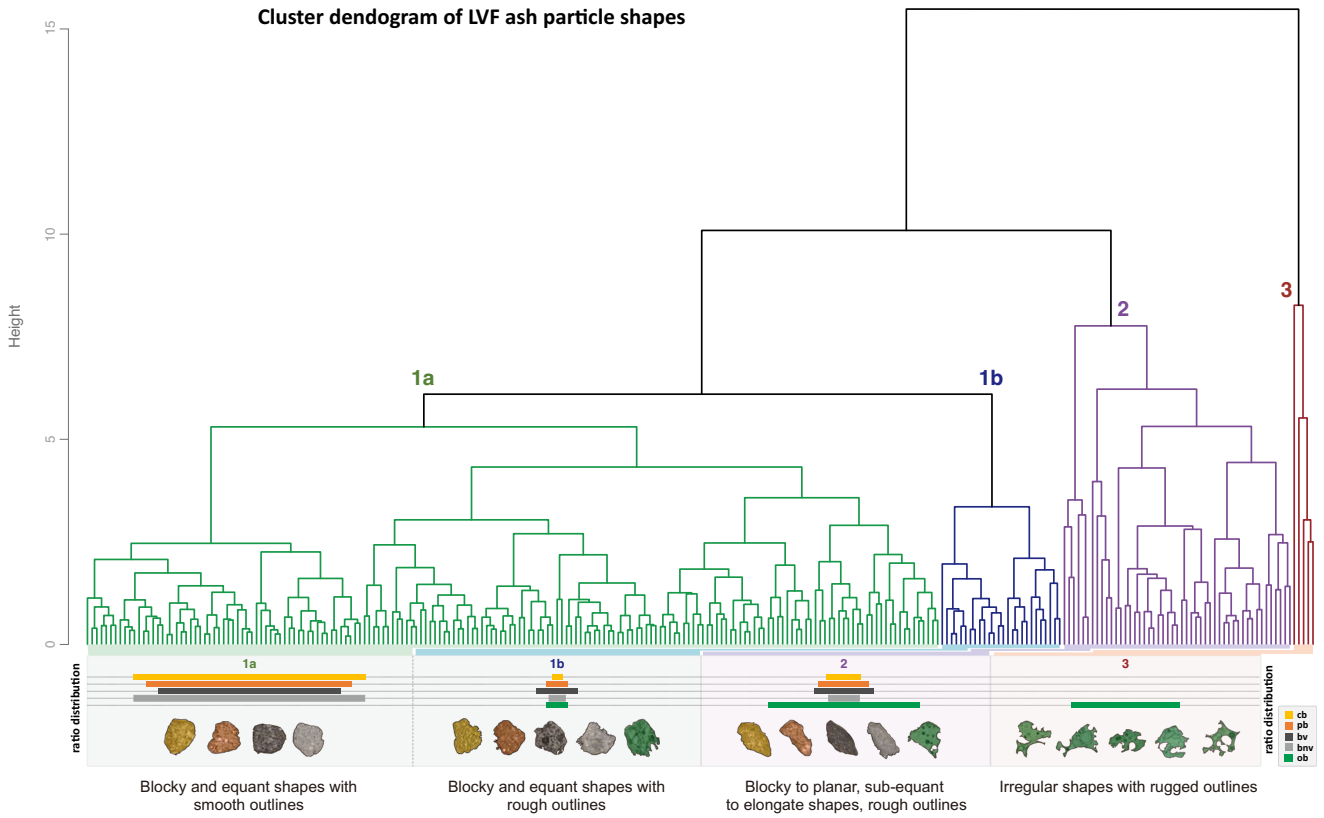

Figure 11: Cluster dendrogram for ash particles from LVF maar complex (n = 266 particles; bnv = 67, pb = 60, bv = 101, cb = 24, ob = 13). The clustering is based on variables of particle analysis (IPA) parameters [Dellino and Volpe 1996] and shape parameters [Liu et al. 2015]. The variables used were Circularity, Rectangularity, Compactness, Elongation, Form Factor, Axial Ratio, Convexity, and Solidity. The images below the cluster show the ratio distribution of the componentry classes and representative particles (from left to right, the images show a change in shape from blocky and equant to sub-equant and elongate to irregular, respectively).

slightly different cooling histories and/or geochemical compositions yield variable textures (bubbles and crystals) and rheological properties, resulting in the different type A component classes in the LVF maars. Yet these magma parcels underwent the same type of fragmentation, resulting in relatively similar shapes (manifested by clusters 1 and 2) regardless of cooling history or geochemical composition. The type B juvenile particles, on the other hand, appear to be from a distinct parcel of magma unique to the northern maars, with higher silica, hotter temperatures, fewer crystals, and larger bubbles, which fragmented into irregular-fluidal shapes, either because these less viscous particles had sufficient time to relax after phreatomagmatic fragmentation or because they underwent magmatic fragmentation.

Principal Component Analysis (PCA) has been applied to morphometric parameters in previous studies by Maria and Carey [2002, 2007] and Nurfiani and Bouvet de Maisonneuve [2018] to investigate eruption styles and depositional processes (e.g. Grímsvötn [hydromagmatic fragmentation] and Katla [magmatic fragmentation]; Mt. Helens 1980 and Tambora 1815 fall, surge, and flow; Surtsey 1963–64, Pacific deep-water seamount; Iwodake, Merapi 2013, and Kelud). Using PCA, we explored the relationship between textural characteristics, rheological properties, and geochemical composition on the morphology of 16 representative samples of juvenile A and B (average values) from the LVF maar complex (Figure 12). To avoid improper mixing of size fractions (125–250 μm grains used for morphology and textural analysis; 0.5–1 mm used for geochemical analysis) and enable direct comparison of the clustering based on each dataset independently. We plotted the first two principal components (PC1 and PC2) separately from each PCA variable (morphometric, morphometric + textural, and geochemistry). Each ash particle class (as defined during componentry) plots in distinct areas on the PC1–PC2 using morphometric (Figure 12A) and morphometric + textural (Figure 12B) variables. Juvenile B particles are interpreted as having a magmatic-like origin, indicating that Circularity, Rectangularity, and Elongation (as well as other morphometric parameters) are among the most discriminating aspects of these grains, which are also geochemically evolved. The juvenile A grains, interpreted as phreatomagmatic, were discriminated by Convexity, Compactness, Solidity, Form Factor, and Aspect Ratio. Geochemically, they are various in composition, but each class has distinct characteristics (Figure 7A–C and Figure 12C). Within juvenile A grains, the PC2 axis using shape and textural variables (Figure 12B) helps differentiate the variety of classes quantitatively. The PC2 axis is more influenced than the PC1 axis by vesicles (vesicular-

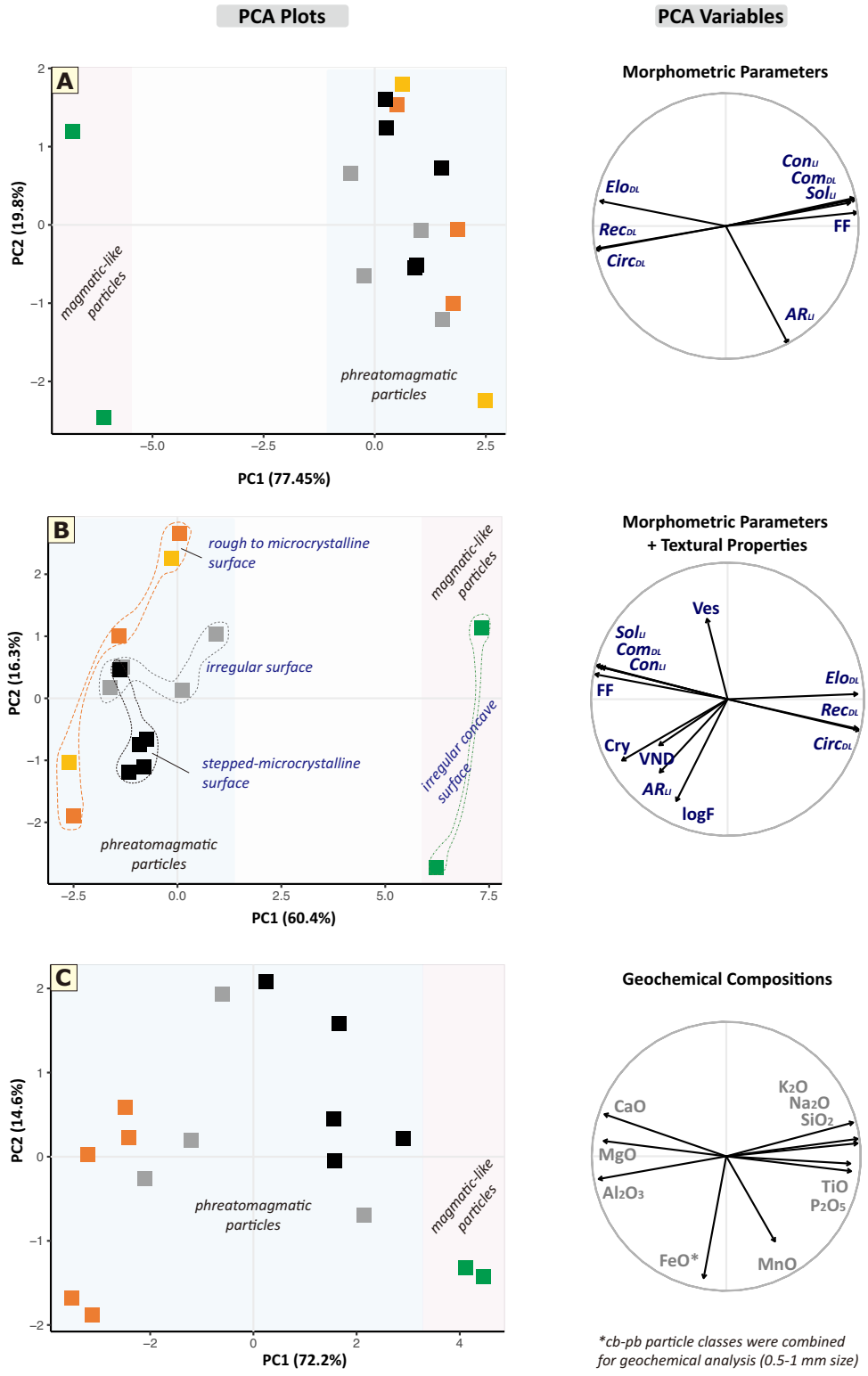

Figure 12: Principal Component Analysis (PCA) of integrated multivariable parameters of ash particles from LVF maar complex, including morphometric parameters [A], morphometric parameters + textural features [B], and geochemistry [C]. The [A] and [B] plots show a clear distinction between particle types, with each plot in the quadrants according to their dominance factors. For example, juvenile B ash particles are located at the high PC1 axis [B] while juvenile A particles are located in the opposite area. Furthermore, phreatomagmatic ash particle (juvenile A) can be divided based on the PC2 axis (mostly by textural variables) in [B], which has relatively low values in bnv ash, moderate values in bv ash, and moderate to high values in cb + pb ash. Two samples of cb-pb plotted in the low values of the PC2 axis [B] related to the high crystallinity feature.

ity, VND), crystals, and viscosity. At the relatively low PC2 end of the spectrum, the bnv grains have relatively higher viscosities, more crystals, are more dense and blocky, and have stepped microcrystalline surfaces. At the high end of the PC2 spectrum, cb and pb particles have relatively lower viscosities, fewer crystals, higher vesicularity, and a mostly blocky shape with an irregular to rough surface (cb + pb + bv). Two grains, one cb and one pb, are plotted at the low end of the PC2 axis, which may be strongly affected by high crystal content (Table 4; 5-12a cb1 and 20-1 pb1 samples). As mentioned in the clustering result, particularly in juvenile type A (phreatomagmatic particles) with mostly blocky shapes, their broad geochemical compositions result in variable textures, rheological properties, and/or cooling histories that may not be as crucial aspects as the fragmentation process to the shapes of this ash type. In addition, the PCA analysis conducted on morphometric and textural parameters (as shown in Figure 12B) offers a quantitative approach to distinguish between distinct ash classes by considering their fragmentation processes and surface characteristics.

Our integrated analytical approach reveals that while the juvenile ash types exhibit variability in composition, their shape distributions principally reflect the predominant brittle fragmentation style of phreatomagmatism. The blocky morphologies of most juvenile A particles, despite their geochemical diversity, indicate that phreatomagmatic processes were the primary control over their shapes. In contrast, the irregular morphology of the juvenile B particles signifies a distinct magmatic fragmentation origin. These findings demonstrate that in the LVF maar complex, variable magma properties yield diverse ash components, yet fragmentation dynamics govern pyroclast shapes.

4.3 Composition of ash particles

In this study, we conducted a geochemical analysis of each class of ash particles to better constrain their origins. By integrating the results of the textural identification with the geochemical data, we were able to infer that the ash particles were derived from a heterogeneous magma source (as depicted in Figure 7A–C). Our findings suggest that brown (cb-pb) (north and west maars) and grayish-black (east maars) ash were formed from the least evolved of low-K to medium-K basaltic magma. The compositions of the black ash (bv + bnv) from the north and west maars were also similar, originating from medium-K to high-K more evolved basalt to basaltic andesite magma. On the other hand, orange-brown (ob) ash particles were found to be derived from a distinctly different batch of magma with a high silica content (primarily in high-K basaltic andesite). The mineral assemblages of the ob class particles were also distinct, with pyroxene and olivine minerals being uncommon (Figure 6). An anomalous iron trend in the PCA geochemistry (Figure 12C) plot towards the low end of the PC2 axis and two different trends of iron concentration versus silica enrichment indicate that there is a specific geochemical pattern between gray + cb-pb and bv + bnv + ob (e.g. different crystal fractionation phases). A possible reason for the steep decreasing trend in gray, cb-pb, and bv particles towards increasing silica is more effective crystallization of the Fe-Ti oxide minerals (average: Fe-Ti oxide abundance in cb-pb [14.6 %] is higher than in bv [8.7 %], bnv [5.9 %], and ob [7.9 %] ash particles: Table 4). The geochemical data from LVF may relate to the magmatic evolution towards a more silicic composition during the progression of eruptions, as noted in other mafic volcanic systems [e.g. Gaunt et al. 2016]. Additionally, the geochemical data from the north scoria cone deposits (average: SiO_2 at 42.3 %; medium-K picrobasaltic) and east lava (Ranu Agung; average: SiO_2 at 45.4 %; medium-K basalt) indicate that they possessed a less evolved composition and could be comparable to the initial magma composition that fed the maar complex of the study area. Further investigation is required into the geochemistry, trace elements, and mineral chemistry of ash particles, lavas, and scoria cone deposits to shed more light on these issues.

5 Conclusion

This study presents a comprehensive analysis of ash particles produced by maar eruptions in the Lamongan Volcanic Field (LVF), providing the first detailed observations of their characteristics. The ash particles can be classified into seven classes based on componentry data and their relation to the maar eruption, which can itself be divided into two main categories: juvenile particles (composed of juvenile A [black non-vesicular, black vesicular, clear-brown, pale-brown] and juvenile B [orange-brown]) and other (free crystals and altered grains). The observed juvenile A particles mostly exhibit typical blocky to planar shapes resulting from phreatomagmatic fragmentation of magma, which produced low vesicularity particles with highly crystalline groundmasses and clear-brown to opaque (brown-black) colors. In contrast, juvenile B particles (ob) have irregular shapes and were produced by magmatic-like fragmentation. The calculated magma viscosity relatively increases from orange (ob) to brown (cp + pb) to black ash particles (bv + bnv) due to magma composition and degree of crystallization.

According to the clustering analysis, phreatomagmatic juvenile A particles predominantly have blocky shapes (84 % in clusters 1a and 1b) and sub-equant shapes (16 % in cluster 2). On the other hand, magmatic-like fragmentation produced mostly irregular juvenile B particles with sub-equant shapes (54 % in cluster 2) and irregular shapes (36 % in cluster 3). From PCA analysis results using morphological parameters, we infer the likely fragmentation process of the ash particles from the LVF maar complex. Most juvenile A particles, despite their geochemical diversity, exhibited blocky shapes, indicating the influence of phreatomagmatic processes. In contrast, juvenile B particles displayed irregular shapes, suggesting a distinct magmatic fragmentation origin. These findings demonstrate how fragmentation dynamics govern pyroclast shapes in the LVF maar complex, despite varying magma properties.

Integrated textural and geochemical analyses show that the LVF maar pyroclasts come from either a mixture of different types of magma or from several batches of magma with slightly different compositions and/or cooling histories. The juvenile type A particles indicate various degrees of differentiation, with brown ash (cb + pb) (north and west maars) and

grayish-black ash (east maars) representing the least evolved basaltic magmas, while the black ash particles (bv + bnv; north and west maars) indicating more evolved basaltic to basaltic andesite magma. In contrast, juvenile B (ob ash particles) with a slightly higher silica content implies further evolution towards basaltic andesite composition. Furthermore, the north scoria cone deposits (average: SiO_2 42.3 %; picrobasaltic) and east lava (Ranu Agung; average: SiO_2 45.4 %; basaltic) exhibit the most mafic-primitive compositions, which could be comparable to the initial magma composition that feeds the maar complex of LVF.

Author Contributions

MAG conceptualized the main research idea, developed the methodology, conducted the fieldwork and laboratory analysis, analyzed the data, and wrote the original manuscript draft. TO handled funding acquisitions, contributed to study design, fieldwork supervision, and manuscript review and editing. AH and TH provided significant insights and discussion during study design, data analysis and interpretation, and manuscript revision. All authors contributed to the reviewing and editing of the final manuscript.

Acknowledgements

The authors acknowledge the financial support received from the Ministry of Education, Culture, Sports, Science, and Technology of Japan (MEXT) scholarship and Akita University for this research work. The authors would like to thank Editor Alison H. Graettinger and three anonymous reviewers for their critical reviews and constructive comments that helped improve the manuscript. The authors also express their gratitude to Y. Hayakawa, R. F. Hasibuan, R. Suhendra, T. Imura, and J. N. Indriyanto for their technical assistance with laboratory work and analytical instruments. The authors would like to extend their appreciation to A. A. Patria, W. N. Hamzah, and M. L. A. Moktikanana for their valuable discussions and acknowledge the officers of Perum Perhutani Klakah and Segaran, K. H. N. Rohman, and M. A. Muzakky for their generous support during the field investigation and sample collection.

Data Availability

All ash particle images and numerical data generated during this study are available online in the supplementary material alongside this article. The ash particle images are available in Supplementary Material File 1. The data used for hierarchical cluster analysis (HCA) are provided in Supplementary Material Table S1. The data used for principal component analysis (PCA) are provided in Supplementary Material Table S2.

Copyright Notice

References

Bagdassarov, N. S. and D. B. Dingwell (1992). "A rheological investigation of vesicular rhyolite". *J. Volcanol. Geotherm. Res.* 50(3), pages 307–322. DOI: 10.1016/0377-0273(92)90099-Y.

Büttner, R., P. Dellino, L. La Volpe, V. Lorenz, and B. Zimanowski (2002). "Thermohydraulic explosions in phreatomagmatic eruptions as evidenced by the comparison between pyroclasts and products from Molten Fuel Coolant Interaction experiments". *Journal of Geophysical Research: Solid Earth* 107(B11), ECV 5-1-ECV 5–14. DOI: 10.1029/2001jb000511.

Carn, S. A. (2000). "The Lamongan volcanic field, East Java, Indonesia: physical volcanology, historic activity and hazards". *Journal of Volcanology and Geothermal Research* 95(1-4), pages 81–108. DOI: 10.1016/s0377-0273(99)00114-6.

Carn, S. A. and D. M. Pyle (2001). "Petrology and Geochemistry of the Lamongan Volcanic Field, East Java, Indonesia: Primitive Sunda Arc Magmas in an Extensional Tectonic Setting?" *Journal of Petrology* 42(9), pages 1643–1683. DOI: 10.1093/petrology/42.9.1643.

Cassidy, M., J. M. Castro, C. Helo, V. R. Troll, F. M. Deegan, D. Muir, D. A. Neave, and S. P. Mueller (2016). "Volatile dilution during magma injections and implications for volcano explosivity". *Geology* 44(12), pages 1027–1030. DOI: 10.1130/g38411.1.

Cioni, R., C. D'Oriano, and A. Bertagnini (2008). "Fingerprinting ash deposits of small scale eruptions by their physical and textural features". *Journal of Volcanology and Geothermal Research* 177(1), pages 277–287. DOI: 10.1016/j.jvolgeores.2008.06.003.

Comida, P. P., P.-S. Ross, T. Dürig, J. D. L. White, and N. Lefebvre (2022). "Standardized analysis of juvenile pyroclasts in comparative studies of primary magma fragmentation: 2. Choice of size fraction and method optimization for particle cross-sections". *Bulletin of Volcanology* 84(1). DOI: 10.1007/s00445-021-01517-5.

D'Oriano, C., A. Bertagnini, R. Cioni, and M. Pompilio (2014). "Identifying recycled ash in basaltic eruptions". *Scientific Reports* 4(1). DOI: 10.1038/srep05851.

D'Oriano, C., R. Cioni, A. Bertagnini, D. Andronico, and P. D. Cole (2011). "Dynamics of ash-dominated eruptions at Vesuvius: the post-512 AD AS1a event". *Bulletin of Volcanology* 73(6), pages 699–715. DOI: 10.1007/s00445-010-0432-1.

Dellino, P. and G. Liotino (2002). "The fractal and multifractal dimension of volcanic ash particles contour: a test study on the utility and volcanological relevance". *Journal of Volcanology and Geothermal Research* 113(1-2), pages 1–18. DOI: 10.1016/s0377-0273(01)00247-5.

Dellino, P. and L. L. Volpe (1996). "Image processing analysis in reconstructing fragmentation and transportation mechanisms of pyroclastic deposits. The case of Monte Pilato-Rocche Rosse eruptions, Lipari (Aeolian islands, Italy)".

Journal of Volcanology and Geothermal Research 71(1), pages 13–29. DOI: 10.1016/0377-0273(95)00062-3.

Dürig, T., M. Bowman, J. White, A. Murch, D. Mele, A. Verolino, and P. Dellino (2018). "PARTIcle Shape ANalyzer PARTISAN – an open source tool for multi-standard two-dimensional particle morphometry analysis". *Annals of Geophysics* 61(Vol 61 (2018)). DOI: 10.4401/ag-7865.

Dürig, T., P.-S. Ross, P. Dellino, J. D. L. White, D. Mele, and P. P. Comida (2021). "A review of statistical tools for morphometric analysis of juvenile pyroclasts". *Bulletin of Volcanology* 83(11). DOI: 10.1007/s00445-021-01500-0.

Gaunt, H. E., B. Bernard, S. Hidalgo, A. Proaño, H. Wright, P. Mothes, E. Criollo, and U. Kueppers (2016). "Juvenile magma recognition and eruptive dynamics inferred from the analysis of ash time series: The 2015 reawakening of Cotopaxi volcano". *Journal of Volcanology and Geothermal Research* 328, pages 134–146. DOI: 10.1016/j.jvolgeores.2016.10.013.

Graettinger, A. (2018). "Trends in maar crater size and shape using the global Maar Volcano Location and Shape (MaarVLS) database". *Journal of Volcanology and Geothermal Research* 357, pages 1–13. DOI: 10.1016/j.jvolgeores.2018.04.002.

Heiken, G. (1978). "Characteristics of tephra from cinder cone, Lassen volcanic National Park, California". *Bulletin Volcanologique* 41(2), pages 119–130. DOI: 10.1007/bf02597025.

Heiken, G. and K. Wohletz (1985). *Volcanic ash*. University Presses of California, Chicago, Harvard & MIT. ISBN: 9780520052413.

Higgins, M. D. (2000). "Measurement of crystal size distributions". *American Mineralogist* 85(9), pages 1105–1116. DOI: 10.2138/am-2000-8-901.

– (2002). "Closure in crystal size distributions (CSD), verification of CSD calculations, and the significance of CSD fans". *American Mineralogist* 87(1), pages 171–175. DOI: 10.2138/am-2002-0118.

Higgins, M. D. and D. Chandrasekharam (2007). "Nature of Sub-volcanic Magma Chambers, Deccan Province, India: Evidence from Quantitative Textural Analysis of Plagioclase Megacrysts in the Giant Plagioclase Basalts". *Journal of Petrology* 48(5), pages 885–900. DOI: 10.1093/petrology/egm005.

Hornby, A., U. Kueppers, B. Mauer, C. Poetsch, and D. Dingwell (2020). "Experimental constraints on volcanic ash generation and clast morphometrics in pyroclastic density currents and granular flows". *Volcanica* 3(2), pages 263–283. DOI: 10.30909/vol.03.02.263283.

Houghton, B. F. and C. J. N. Wilson (1989). "A vesicularity index for pyroclastic deposits". *Bulletin of Volcanology* 51(6), pages 451–462. DOI: 10.1007/bf01078811.

Jordan, S. C. (2013). "Factors controlling the formation of a very large maar volcano and the fragmentation process in phreatomagmatic eruptions: Lake Purrumbete Maar, southeastern Australia". PhD thesis. Monash University.

Jordan, S. C., T. Dürig, R. A. F. Cas, and B. Zimanowski (2014). "Processes controlling the shape of ash particles: Results of statistical IPA". *Journal of Volcanology and Geothermal Research* 288, pages 19–27. DOI: 10.1016/j.jvolgeores.2014.09.012.

Klein, J., S. P. Mueller, C. Helo, S. Schweitzer, L. Gurioli, and J. M. Castro (2018). "An expanded model and application of the combined effect of crystal-size distribution and crystal shape on the relative viscosity of magmas". *Journal of Volcanology and Geothermal Research* 357, pages 128–133. DOI: 10.1016/j.jvolgeores.2018.04.018.

Kueppers, U., C. Putz, O. Spieler, and D. B. Dingwell (2012). "Abrasion in pyroclastic density currents: Insights from tumbling experiments". *Physics and Chemistry of the Earth, Parts A/B/C* 45–46, pages 33–39. DOI: 10.1016/j.pce.2011.09.002.

Liu, E., K. Cashman, and A. Rust (2015). "Optimising shape analysis to quantify volcanic ash morphology". *GeoResJ* 8, pages 14–30. DOI: 10.1016/j.grj.2015.09.001.

Lorenz, V. (1986). "On the growth of maars and diatremes and its relevance to the formation of tuff rings". *Bulletin of Volcanology* 48(5), pages 265–274. DOI: 10.1007/bf01081755.

Lorenz, V., P. Suhr, and S. Suhr (2017). "Phreatomagmatic maar-diatreme volcanoes and their incremental growth: a model". *Geological Society, London, Special Publications* 446(1), pages 29–59. DOI: 10.1144/sp446.4.

Mader, H., E. Llewellin, and S. Mueller (2013). "The rheology of two-phase magmas: A review and analysis". *Journal of Volcanology and Geothermal Research* 257, pages 135–158. DOI: 10.1016/j.jvolgeores.2013.02.014.

Manga, M., A. Patel, and J. Dufek (2011). "Rounding of pumice clasts during transport: field measurements and laboratory studies". *Bulletin of Volcanology* 73(3), pages 321–333. DOI: 10.1007/s00445-010-0411-6.

Maria, A. and S. Carey (2002). "Using fractal analysis to quantitatively characterize the shapes of volcanic particles". *Journal of Geophysical Research: Solid Earth* 107(B11), ECV 7-1-ECV 7–17. DOI: 10.1029/2001jb000822.

– (2007). "Quantitative discrimination of magma fragmentation and pyroclastic transport processes using the fractal spectrum technique". *Journal of Volcanology and Geothermal Research* 161(3), pages 234–246. DOI: 10.1016/j.jvolgeores.2006.12.006.

Mattsson, H. B. (2010). "Textural variation in juvenile pyroclasts from an emergent, Surtseyan-type, volcanic eruption: The Capelas tuff cone, São Miguel (Azores)". *Journal of Volcanology and Geothermal Research* 189(1–2), pages 81–91. DOI: 10.1016/j.jvolgeores.2009.10.007.

Miwa, T., N. Geshi, and H. Shinohara (2013). "Temporal variation in volcanic ash texture during a vulcanian eruption at the Sakurajima volcano, Japan". *Journal of Volcanology and Geothermal Research* 260, pages 80–89. DOI: 10.1016/j.jvolgeores.2013.05.010.

Morales Volosín, S. and C. Risso (2019). "El Pozo Volcanic Complex: Evolution of a group of maars, central Mendoza province, Argentina". *Journal of Volcanology and Geothermal Research* 371, pages 177–191. DOI: 10.1016/j.jvolgeores.2019.01.005.

Morgan, D. J. and D. A. Jerram (2006). "On estimating crystal shape for crystal size distribution analysis". *Journal of Volcanology and Geothermal Research* 154(1-2), pages 1–7. DOI: 10.1016/j.jvolgeores.2005.09.016.

Murtagh, R. M. and J. D. L. White (2013). "Pyroclast characteristics of a subaqueous to emergent Surtseyan eruption, Black Point volcano, California". *Journal of Volcanology and Geothermal Research* 267, pages 75–91. DOI: 10.1016/j.jvolgeores.2013.08.015.

Németh, K. (2010). "Volcanic glass textures, shape characteristics and compositions of phreatomagmatic rock units from the Western Hungarian monogenetic volcanic fields and their implications for magma fragmentation". *Open Geosciences* 2(3). DOI: 10.2478/v10085-010-0015-6.

Németh, K. and S. Kósik (2020). "Review of Explosive Hydrovolcanism". *Geosciences* 10(2), page 44. DOI: 10.3390/geosciences10020044.

Noguchi, S., A. Toramaru, and S. Nakada (2008). "Relation between microlite textures and discharge rate during the 1991–1995 eruptions at Unzen, Japan". *Journal of Volcanology and Geothermal Research* 175(1–2), pages 141–155. DOI: 10.1016/j.jvolgeores.2008.03.025.

Nurfiani, D. and C. Bouvet de Maisonneuve (2018). "Furthering the investigation of eruption styles through quantitative shape analyses of volcanic ash particles". *Journal of Volcanology and Geothermal Research* 354, pages 102–114. DOI: 10.1016/j.jvolgeores.2017.12.001.

Pardo, N., S. J. Cronin, K. Németh, M. Brenna, C. I. Schipper, E. Breard, J. D. White, J. Procter, B. Stewart, J. Agustín-Flores, A. Moebis, A. Zernack, G. Kereszturi, G. Lube, A. Auer, V. Neall, and C. Wallace (2014). "Perils in distinguishing phreatic from phreatomagmatic ash; insights into the eruption mechanisms of the 6 August 2012 Mt. Tongariro eruption, New Zealand". *Journal of Volcanology and Geothermal Research* 286, pages 397–414. DOI: 10.1016/j.jvolgeores.2014.05.001.

Proussevitch, A. A., D. L. Sahagian, and W. D. Carlson (2007). "Statistical analysis of bubble and crystal size distributions: Application to Colorado Plateau basalts". *Journal of Volcanology and Geothermal Research* 164(3), pages 112–126. DOI: 10.1016/j.jvolgeores.2007.04.006.

Rausch, J., B. Grobéty, and P. Vonlanthen (2015). "Eifel maars: Quantitative shape characterization of juvenile ash particles (Eifel Volcanic Field, Germany)". *Journal of Volcanology and Geothermal Research* 291, pages 86–100. DOI: 10.1016/j.jvolgeores.2014.11.008.

Ross, P.-S., T. Dürig, P. P. Comida, N. Lefebvre, J. D. L. White, D. Andronico, S. Thivet, J. Eychenne, and L. Gurioli (2022). "Standardized analysis of juvenile pyroclasts in comparative studies of primary magma fragmentation; 1. Overview and workflow". *Bulletin of Volcanology* 84(1). DOI: 10.1007/s00445-021-01516-6.

Ross, P.-S. and J. D. L. White (2012). "Quantification of vesicle characteristics in some diatreme-filling deposits, and the explosivity levels of magma–water interactions within diatremes". *Journal of Volcanology and Geothermal Research* 245–246, pages 55–67. DOI: 10.1016/j.jvolgeores.2012.07.006.

Saucedo, R., J. L. Macías, Y. Z. E. Ocampo-Díaz, W. Gómez-Villa, E. Rivera-Olguín, R. Castro-Govea, J. M. Sánchez-Núñez, P. W. Layer, J. R. Torres Hernández, and G. Carrasco-Núñez (2017). "Mixed magmatic–phreatomagmatic explosions during the formation of the Joya Honda maar, San Luis Potosí, Mexico". *Geological Society, London, Special Publications* 446(1), pages 255–279. DOI: 10.1144/sp446.11.

Schipper, C. I. (2009). "Explosive Submarine Volcanism at Lōihi Seamount, Hawaii". PhD thesis.

Shea, T., B. F. Houghton, L. Gurioli, K. V. Cashman, J. E. Hammer, and B. J. Hobden (2010). "Textural studies of vesicles in volcanic rocks: An integrated methodology". *Journal of Volcanology and Geothermal Research* 190(3–4), pages 271–289. DOI: 10.1016/j.jvolgeores.2009.12.003.

Sheridan, M. F. and K. H. Wohletz (1983). "Hydrovolcanism: Basic considerations and review". *Journal of Volcanology and Geothermal Research* 17(1-4), pages 1–29. DOI: 10.1016/0377-0273(83)90060-4.

Smith, I. E. M. and K. Németh (2017). "Source to surface model of monogenetic volcanism: a critical review". *Geological Society, London, Special Publications* 446(1), pages 1–28. DOI: 10.1144/sp446.14.

Suwarti, T. and Suharsono (1992). "Geological map of the Lumajang and Probolinggo Quadrangle, Java." *Geological Research and Development Centre of Indonesia.* [Map scale 1:100,000.

Valentine, G. A., J. D. L. White, P.-S. Ross, A. H. Graettinger, and I. Sonder (2017). "Updates to Concepts on Phreatomagmatic Maar-Diatremes and Their Pyroclastic Deposits". *Frontiers in Earth Science* 5. DOI: 10.3389/feart.2017.00068.

White, J. D. L. and B. F. Houghton (2006). "Primary volcaniclastic rocks". *Geology* 34(8), page 677. DOI: 10.1130/g22346.1.

White, J. D. L. and P.-S. Ross (2011). "Maar-diatreme volcanoes: A review". *Journal of Volcanology and Geothermal Research* 201(1–4), pages 1–29. DOI: 10.1016/j.jvolgeores.2011.01.010.

White, J. D. L. and G. A. Valentine (2016). "Magmatic versus phreatomagmatic fragmentation: Absence of evidence is not evidence of absence". *Geosphere* 12(5), pages 1478–1488. DOI: 10.1130/ges01337.1.

Wohletz, K. H. and M. F. Sheridan (1983). "Hydrovolcanic explosions; II, Evolution of basaltic tuff rings and tuff cones". *American Journal of Science* 283(5), pages 385–413. DOI: 10.2475/ajs.283.5.385.

Zimanowski, B., G. Fröhlich, and V. Lorenz (1991). "Quantitative experiments on phreatomagmatic explosions". *Journal of Volcanology and Geothermal Research* 48(3-4), pages 341–358. DOI: 10.1016/0377-0273(91)90050-a.